European Journal of Mechanics / B Fluids 120 (2026) 204592

Contents lists available at ScienceDirect

European Journal of Mechanics / B Fluids

journal homepage: www.elsevier.com/locate/ejmflu

Mean flow and turbulence anisotropy representation in a round jet impingement: Experiment, DNS and modeling

M. Bopp [a], T. Häber [b,*], F. Secchi [c], S. Schulz [d], S. Wegt [a], L. Krüger [a], R. Suntz [b], D. Trimis [d], B. Frohnapfel [c], S. Jakirlić [a]

[a] Institute of Fluid Mechanics and Aerodynamics, Technical University of Darmstadt, Peter-Grünberg-Straße 10, 64287 Darmstadt, Germany
[b] Institute for Chemical Technology and Polymer Chemistry, Karlsruhe Institute of Technology, Engesserstraße 18, 76131 Karlsruhe, Germany
[c] Institute of Fluid Mechanics, Karlsruhe Institute of Technology, Kaiserstraße 10, 76131 Karlsruhe, Germany
[d] Engler-Bunte-Institute, Chair for Combustion Technology, Karlsruhe Institute of Technology, Engler-Bunte-Ring 7, 76131 Karlsruhe, Germany

ARTICLE INFO

Keywords:
Round jet impingement
Particle Image Velocimetry
Direct Numerical Simulation
Scale-resolving RANS-based model
Subscale stress tensor model
Reynolds stress anisotropy representation
Barycentric coloring

ABSTRACT

The present study examines a round jet exiting a circular tube at a diameter-based Reynolds number of Re_b = 10000, impinging perpendicularly on a smooth wall. In addition to Particle Image Velocimetry (PIV) measurements and Direct Numerical Simulation (DNS) based on the spectral element method, a sensitized eddy-resolving RANS (Reynolds-Averaged Navier Stokes) approach with a differential Reynolds stress model (RSM) mimicking a subscale model was applied to generate a flow database comparable across multiple methods. Within the framework of the scale-resolving RANS–RSM, the turbulent correlations governing the dynamics of the entire subscale stress tensor are obtained as solutions to an appropriately extended set of RANS-based model equations that describe the evolution of the corresponding turbulence quantities. The representative subscale turbulent length and time scales that constitute the relationships entering the relevant equations of motion are determined by using the unresolved residual part of the turbulence kinetic energy and its viscous dissipation rate. The detailed mean flow and associated turbulence correlations, evaluated together with some global characteristics (e.g., wall shear stress), enabled a deeper insight into the topological flow properties and facilitated a critical assessment of the modeling approach through direct comparison with the complementary experiment and direct numerical simulation. Additionally, the study contributes to turbulence anisotropy characterization based on three-dimensional mapping of Reynolds stress anisotropy properties using Lumley's classical representation of anisotropy invariants as well as barycentric coloring. The two-component invariant parameter field exhibits fairly high, close-to-unity values, indicating a weak level of anisotropy consistent with the conditions that characterize the destabilizing effect of strong local streamwise curvature in flows subjected to stagnation. The turbulence structure is constrained within the range between the three-component and two-component isotropic bounds, which underlies the axisymmetric contraction state of turbulence, consistent with the negative values of the third invariant of Reynolds stress anisotropy.

1. Introduction

Wall-impinging flows represent a fundamental configuration in fluid dynamics, combining intricate flow physics with broad engineering relevance. From a fluid mechanics perspective, wall-normal impinging jets exhibit highly complex straining with variable directional orientation, driven by alternating deceleration and acceleration as the free jet impacts the wall, bends, and transitions into a wall-attached jet. This process involves a sign change in the velocity gradient and pronounced streamline curvature, both of which promote intense turbulence generation and strongly non-equilibrium flow behavior. A notable feature of this configuration is the transformation of the streamwise Reynolds stress component in the incoming jet into a wall-normal component within the impingement region. The structural properties of an impinging jet are governed by several operating parameters, most notably the Reynolds number of the incoming jet, the velocity profile form at the pipe exit and the associated turbulence quantities, as well as the nozzle-to-wall distance. These distinctive characteristics, combined with the geometric simplicity of the setup, make the perpendicular impinging jet an exceptionally suitable benchmark for turbulence model validation.

* Corresponding author.
E-mail addresses: thomas.haeber@kit.edu (T. Häber), dimosthenis.trimis@kit.edu (D. Trimis), bettina.frohnapfel@kit.edu (B. Frohnapfel), jakirlic@sla.tu-darmstadt.de (S. Jakirlić).

https://doi.org/10.1016/j.euromechflu.2026.204592
Received 28 October 2025; Received in revised form 8 May 2026; Accepted 22 June 2026
Available online 26 June 2026

Consequently, a substantial body of experimental and computational studies has been reported in the literature. Computational investigations, in particular, have examined the predictive performance of turbulence modeling schemes within the Reynolds-averaged Navier–Stokes (RANS) framework. One of the most frequently studied benchmark cases — representing a round jet impinging perpendicularly onto a wall operating at different Reynolds numbers (Re_D = 23000 and 70000) and nozzle-to-wall distances (z/D = 2 and 6, respectively) — is the early experimental work of Cooper et al. [1], which provides profiles of mean velocity and Reynolds stress components in the central vertical plane at selected locations within the immediate impact region and the wall jet. Complementing these experiments, an extensive RANS model validation study, including both eddy-viscosity models and differential Reynolds stress models, was conducted by Craft et al. [2]. A comprehensive overview of turbulence modeling strategies applied to various impingement configurations is provided by Bopp et al. [3].

The shear layer between the free jet emerging from the pipe-like nozzle, the impingement zone, and the developing wall jet interacting with the entraining ambient fluid exhibits pronounced unsteadiness. While, for example, turbulent length scales in globally stable, wall-parallel flows are typically assumed to be proportional to the distance from the wall, in the near-wall region of an impinging jet, these scales are significantly affected by those generated during the highly unsteady impingement process. This complexity makes scale-resolving simulation techniques particularly well suited for capturing both transient turbulent fluctuations and the mean flow characteristics obtained through time averaging. Accordingly, Large-Eddy Simulation (LES) and Direct Numerical Simulation (DNS), resolving adequately the fluctuating flow dynamics and associated processes of impinging jet configurations, are generally more suitable than Reynolds-averaged Navier–Stokes (RANS) models for accurately reproducing the time-averaged flow field, as RANS approaches often suffer from excessive turbulence production in the immediate impingement region due to incorrect reproduction of the effects associated with the turbulence-enhancing streamline curvature effects (cf. [3]). For a comprehensive understanding of the underlying flow characteristics, including vortical structures and turbulence statistics, the LES studies by Hadžiabdić and Hanjalić [4], which simulate the lower-Reynolds-number case investigated experimentally by [1], as well as by Dairay et al. [5] may be consulted. In addition, DNS studies by Hattori and Nagano [6] and Dairay et al. [7] provide further insight, although they are based on comparatively moderate flow Reynolds numbers (on the order of 10000). The work of Hattori and Nagano [6], in particular, considers a slot jet impingement configuration examined at different nozzle-to-plate distances. Despite the considerable number of published studies on impinging jets, relatively few provide a comprehensive mapping of the full three-dimensional flow topology.

In this context, the present study conducts a comparative evaluation of the predictive performance of two computational approaches — Direct Numerical Simulation (DNS) and a novel scale-resolving, sensitized extension of a differential, near-wall Reynolds stress model — supplemented by a complementary reference experiment, thereby enriching the currently available data sets. Accordingly, the objective of the present study can be summarized as follows:

- A comprehensive three-dimensional representation of the flow pattern, focusing on the development of the mean velocity field and the corresponding Reynolds stress components, with particular emphasis on the characterization of Reynolds stress anisotropy. This is achieved through the representation of characteristic turbulence states in terms of anisotropy invariants. Both the classical Lumley anisotropy invariant theory, [8], and the barycentric coloring method — generally based on the eigenvalues of the Reynolds stress tensor [9,10] — are employed. This approach enables the projection of characteristic turbulent states from the anisotropy triangle directly onto the flow domain. This constitutes an important outcome of the present study, as it provides insight into turbulence anisotropy based on the fundamental physics of the flow under consideration.

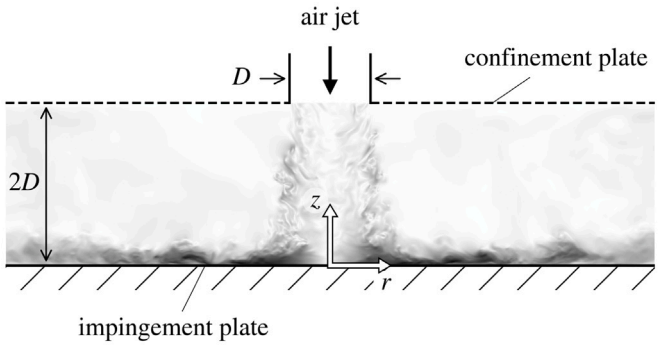

Fig. 1. Schematic of the considered axisymmetric impinging jet setup, showing its layout in the central vertical $r - z$ plane.

- Advancement of a RANS-based, scale-resolving turbulence model through systematic validation, supported by results from complementary experimental investigations and direct numerical simulations (DNS), with particular emphasis on accurately representing near-wall effects. The turbulence model employed in this work represents a novel eddy-resolving unsteady RANS approach and can be characterized as a 'sensitized RANS' methodology. The underlying formulation is based on a near-wall Reynolds stress closure, combined with an exact asymptotic representation of the two-component limiting behavior of turbulence quantities near solid boundaries.

2. Configuration description

The flow configuration investigated presently by means of the Particle Image Velocimetry, Direct Numerical Simulation and a RANS-based turbulent fluctuations-resolving model, represents an incompressible, axisymmetric jet impinging perpendicularly onto a smooth wall, Fig. 1.

Fig. 1 shows an overview of the flow configuration. All investigations are performed with a fully-developed turbulent airflow at a bulk Reynolds number of $\mathrm{Re} = U_\mathrm{b} D/\nu = 10000$,[1] exiting a circular inlet pipe with a diameter D and a bulk inlet velocity of U_b, at ambient pressure. The impingement plate is located at a distance of $2D$ from the nozzle exit, with a radial extent of at least $6D$ in radial direction. The exact size of the radially extended domain varies between numerical and experimental methods, and the differences are detailed in the following sections. To facilitate the computational effort associated with possible low-intensity air entrainment, a confinement plate is placed in the plane of the pipe exit in all simulations. Given the rather large distance between the nozzle and the impact wall, this certainly does not affect the flow in the impingement area of interest. The good agreement between the computational and experimental results at the (r, $z = 2D$) plane confirms this assumption (see Section 4).

The coordinate origin is placed at the center of the impingement plate, with the z-axis pointing away from the wall toward the nozzle exit. Fig. 1 uses the flow configuration representation commonly found in the literature, in which the jet hits the impingement plate from above. In any case, the numerical simulations do not consider thermal

[1] The flow Reynolds number is likewise representative of conditions encountered at the piston surface during the compression stroke of a motored internal combustion (IC) engine, characterized by a qualitatively similar flow pattern that includes streamline curvature effects, varying pressure gradients, and, consequently, non-fully developed, wall-jet-like boundary layers (see, e.g., Fig. 1 in [11]). It is recalled that Reynolds numbers associated with piston speeds — representing the effective flow velocity within the cylinder — are typically on the order of 10^4 for engine speeds between 400 and 800 *rpm* (see, e.g., [12]).

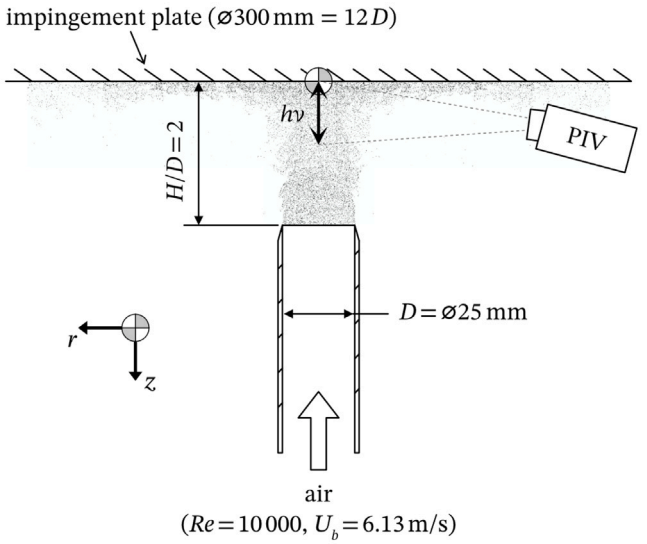

Fig. 2. Schematic overview of the experimental setup for the PIV measurements. The actual test setup used is shown here, with the jet hitting the impingement plate from below, in contrast to the usual representation of the impinging jet setup shown in Fig. 1. No confinement plate is used at the nozzle exit to facilitate optical access to both the nozzle exit and the near-wall area with the same Scheimpflug orientation (see the text for details).

fields or potential buoyancy forces; therefore, the actual orientation has no influence on the results. In the following analysis, only flow fields and their statistics that are averaged in time and spatially over the circumferential coordinate are considered; thus, the radial coordinate r is used to denote the radial direction. However, all simulations are performed on a three-dimensional, appropriately meshed flow domain, without exploiting the rotational symmetry of the configuration.

3. Methodology

3.1. Particle Image Velocimetry (PIV)

The experimental setup of the axially symmetric impingement jet configuration is shown in Fig. 2. The nozzle is a circular, seamless stainless-steel tube with an inner diameter of $D = 25\,\text{mm}$ ($\pm 0.25\,\text{mm}$) and a length of $L = 1300\,\text{mm} \approx 52D$. The inlet tube length ensures fully developed turbulent pipe flow at the jet exit, thereby providing well-defined inlet conditions for the axisymmetric jet. The air temperature is maintained at $293\,\text{K}$. The air mass flow rate is regulated using a thermal mass flow controller (Bronkhorst F-203AV or MKS G250 A). A perforated plate with an open area ratio of 50% is installed at the nozzle inlet to rectify the flow. No confinement plate is placed at the nozzle exit, allowing unobstructed optical access to the nozzle-exit and near-wall region without altering the camera arrangement. This configuration enables control of the outlet conditions immediately before or during each measurement series near the wall, thereby ensuring the reproducibility of the inlet conditions. Downstream of the nozzle exit, the jet develops freely and impinges on the target plate after a distance of $2D = 50\,\text{mm}$. The impingement plate, with a diameter of $12D$ ($= 300\,\text{mm}$), is made of aluminum and maintained at the same temperature as the air jet. The entire setup is mounted on an xyz translation stage, allowing high-resolution imaging of different regions of the impinging jet while keeping the laser sheet and camera fixed.

Velocity fields are measured using particle imaging velocimetry (PIV) [13]. The illumination is provided by a frequency-doubled, double-cavity Nd:YAG laser (Spectra Physics PIV 100), which emits two pulses with a variable delay Δt at a repetition rate of 10 Hz. The laser light sheet is formed by a cylindrical lens system, yielding a height of

Table 1
Field of view (FOV), time delay Δt between PIV double images, final correlation window size, and resulting vector resolution used in the PIV measurements.

FOV [mm^2]	Δt [μs]	window size [–]	vector res. [μm]
37.8 × 32.2	25, 35	24 × 24	89
20.7 × 17.7	15	32 × 32	65
17.9 × 15.2	15	32 × 32	56

$\approx 40\,\text{mm}$ and a thickness of $\approx 65\,\mu\text{m}$ (defined at the $1/e^2$ radius) at the waist. The air stream is seeded with di-ethyl-hexyl-sebacate (DEHS) oil droplets generated by a seeding unit (Palas AFG 10), producing droplets with an averaged mean diameter of $0.5\,\mu\text{m}$ and a size selectivity of $< 10\,\mu\text{m}$. The scattered light is recorded by an sCMOS camera (LaVision sCMOS Imager) with 2560 × 2160 pixels and a 16-bit analog-to-digital converter. A Nikon 105 mm $f/1.8$ objective lens is used for imaging, with extension rings of 12 mm, 36 mm, and 48 mm applied to achieve different spatial resolutions and fields of view. The camera and laser sheet are arranged in a Scheimpflug configuration (viewing angle ≈ 2–3°) to minimize spatial clipping of the scattered light by the wall and to enable measurements very close to the wall.

Commercial software (LaVision DaVis 10) is employed for image acquisition, parameter setting, perspective correction, and image correlation. The time delay between double-frame images is adjusted according to the chosen correlation window size and the velocity range observed in the experiment. Table 1 summarizes the combinations of field of view (FOV), inter-frame time delay Δt, final correlation window size, and resulting vector resolution used in the measurements. Image correlation is carried out in four passes, with the initial window size set to twice the final size and a window overlap of 75%. The independence of the resulting velocity fields from interrogation window size and inter-frame time delay Δt was verified in preliminary tests.

Due to factors such as out-of-plane particle motion or non-uniform particle scattering, the image correlation technique inevitably produces erroneous vectors, see e.g. [14]. This must be considered when evaluating the Reynolds stress components, since variance and covariance are not robust measures of distribution width from a statistical perspective and are strongly affected by outliers [15]. To avoid introducing bias into the data set, no digital image filters or correction routines (e.g., vector interpolation [16]) available in the DaVis software are applied. Instead, erroneous vectors are treated as outliers and removed entirely from the data set by calculating pixel-wise statistics for each series of vector images. Fig. 3 (upper) shows a sample time trace of the u_z component along the nozzle axis at 1 mm above the nozzle exit, where outliers are marked with red circles. Outlier detection is based on the robust and widely used interquartile range (IQR), defined as the difference between the 25th (q_{25}) and 75th (q_{75}) percentiles [17]. If any vector component deviates from q_{25} or q_{75} by more than $1.5 \times \text{IQR}$ (gray-shaded area), the entire vector is classified as an outlier and removed.

To illustrate the bias introduced by erroneous vectors, Fig. 3 (lower) presents the variance of the wall-normal velocity component at the nozzle exit, calculated both with outliers included (red points) and after their removal (black points). The spread in the computed variances is markedly reduced once outliers are excluded. As outliers invariably increase variance, the values obtained without them, as expected, lie at the lower bound of the scatter range observed when outliers are included.

Each measurement series typically consists of 1000 vector fields, and in some cases up to 2000. The PIV data presented in this paper comprise eight independent measurement sets, which differ in field of view, inter-frame delay Δt, the mass flow controller used, and multiple re-alignments of the optical setup to assess systematic errors. The bulk velocity U_b is determined individually for each measurement by integrating the outlet velocity profile and varies by less than 3.5% across

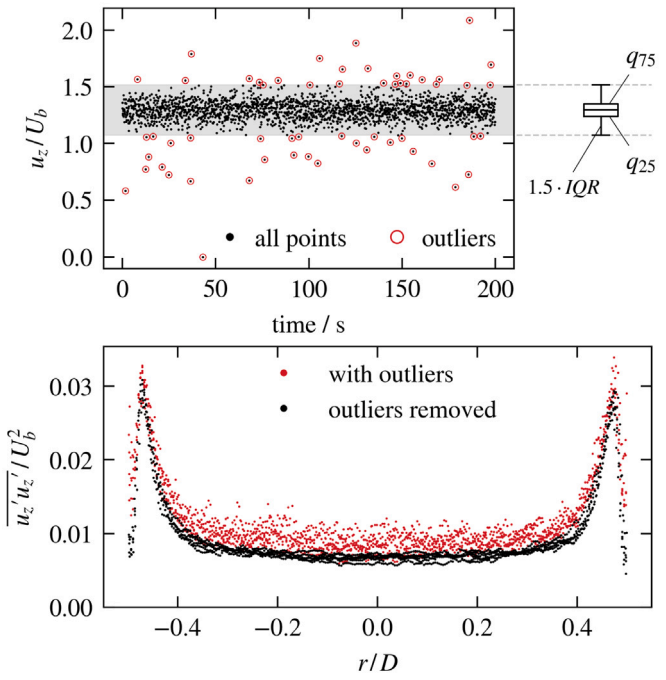

Fig. 3. Upper: Definition and illustration of outliers using a PIV time series at a single point near the pipe exit ($r/D = 0$). Outliers are identified as velocity vectors whose components deviate from the median by more than $1.5 \times$ IQR, where IQR $= q_{75} - q_{25}$ is the interquartile range defined by the lower (q_{25}) and upper (q_{75}) quartiles. Lower: Effect of outliers on the variance, exemplified by the axial velocity component $\overline{u_z' u_z'}/U_b^2$. Excluding outliers markedly reduces the uncertainty of the statistical quantities.

all cases, consistent with the accuracy of the mass flow controllers. All velocities reported hereafter are normalized by the respective bulk velocity. Based on statistical analysis at the nozzle exit, the confidence interval of the mean velocity component is below 1.5% (depending on turbulence level), while the root-mean-square values exhibit confidence intervals between −7 and +15% at a 99% confidence level.

3.2. Eddy-resolving RANS framework

The Reynolds-Averaged Navier–Stokes equations, employed within a time-accurate computational framework governing the flow in the jet impingement configuration underlying the sensitized, eddy-resolving modeling approach, are expressed in Cartesian coordinates as follows::

$$\frac{\partial U_i}{\partial t} + \frac{\partial (U_i U_j)}{\partial x_j} = -\frac{1}{\rho}\frac{\partial p}{\partial x_i} + \frac{\partial}{\partial x_j}\left[\nu\left(\frac{\partial U_i}{\partial x_j}\right) - \overline{u_i' u_j'}\right] \tag{1}$$

The momentum equation presented above corresponds to a RANS-type formulation, but it governs the instantaneous velocity field ($U_i \rightarrow f(x_i, t)$; it applies also to the pressure field) rather than the conventional time-averaged one. In the standard, inherently steady RANS framework, the Reynolds stress tensor $\overline{u_i' u_j'}$ fully represents the turbulence spectrum and is a time-averaged quantity by definition. In the presently used turbulence sensitization procedure, however, this tensor, now depending on time ($\overline{u_i' u_j'} \rightarrow f(x_i, t)$), is redefined: it no longer captures the total (fully modeled) turbulence but instead describes only the dynamics of the unresolved turbulent motions. The dominant turbulence contribution — originating from convective transport in the momentum equation — is explicitly resolved. As a result, the instantaneous velocity field can be decomposed into resolved and fluctuating components in a manner similar to Large Eddy Simulation (LES). A key advantage over a conventional Smagorinsky-type LES and eddy-viscosity-based hybrid RANS/LES models is that the modeled fluctuating contributions to all six turbulent stress components are computed directly from the corresponding transport equations governing the residual turbulence stress tensor:

$$\frac{\mathrm{D}\overline{u_i' u_j'}}{\mathrm{D}t} = P_{ij} + \Phi_{ij} - \varepsilon_{ij}^{\mathrm{h}} + 0.5 D_{ij}^{\nu} + D_{ij}^{p'} + D_{ij}^{u'} \tag{2}$$

Within this framework, the individual contributions of fine-scale stress components to the unresolved turbulent kinetic energy are explicitly captured by solving their respective evolution equations, thereby accounting for the distinct effects on turbulence anisotropy to be represented in a selective and physically consistent manner. The model is formulated as a near-wall approach, implying that the structural properties of the model terms ensure an asymptotically correct representation of near-wall behavior of the mean flow and turbulence quantities. This enables an accurate resolution of the viscosity-affected near-wall region. The formulation is consistent with the well-established understanding that solid walls influence turbulence through non-uniform damping and wall-blocking effects, which act differently on each component of the stress tensor, as reflected in the distributions of the individual stress components (cf. [18]). On the right-hand side of the stress transport equation, the source terms represent several distinct physical processes: the exactly treated production rate P_{ij}, the redistribution term Φ_{ij}, the homogeneous viscous stress-dissipation correlation ε_{ij}^{h}, and various diffusion contributions arising from viscous effects, as well as pressure (p') and velocity (u') fluctuations, $D_{ij}^{(\nu+p'+u')}$. Among these, the molecular diffusion D_{ij}^{ν}, and the production rate are computed without modeling approximations. All remaining processes must be represented through suitable turbulence models. In contrast to a conventional RANS Reynolds stress model — which cannot resolve the spectral dynamics of turbulence — the present IISRSM approach, termed as the Improved Instability-Sensitive Reynolds Stress Model, constitutes a scale-resolving formulation. This enhancement enables it to more faithfully capture turbulent fluctuations across relevant scales. The sensitized RANS model yields an accurately resolved instantaneous flow field, from which time-averaging is subsequently applied to extract the mean flow properties. Consequently, the Reynolds stress components emerging from this modeling approach (see Section 4) contain both the resolved and modeled parts, in contrast to LES, which accounts only for the resolved portion.

The scale-resolving capability of the model is incorporated in conjunction with the Scale-Adaptive Simulation (SAS) methodology proposed by Menter and Egorov [19]. Within this framework, an additional production term P_{IISRSM} is introduced into the transport equation governing the homogeneous part of the specific dissipation rate $\omega^{\mathrm{h}} = \varepsilon^{\mathrm{h}}/k$, where the homogeneous dissipation is defined as $\varepsilon^{\mathrm{h}} = \varepsilon - 0.5 D_{\mathrm{k}}^{\nu}$ and the turbulent kinetic energy is $k = 0.5\overline{u_i' u_i'}$:

$$\left(\frac{\mathrm{D}\omega^{\mathrm{h}}}{\mathrm{D}t}\right)_{\mathrm{IISRSM}} = \left(\frac{\mathrm{D}\omega^{\mathrm{h}}}{\mathrm{D}t}\right)_{\mathrm{RSM}} + P_{\mathrm{IISRSM}} \tag{3}$$

with

$$P_{\mathrm{IISRSM}} = 0.12 \max\left(1.755\kappa\sqrt{k}\left|\nabla^2 \mathrm{U}\right| - T_2, 0\right);$$
$$T_2 = 3\,k\,\max\left[\frac{1}{k^2}(\nabla k)^2, \frac{1}{\omega_h^2}(\nabla \omega_h)^2\right] \tag{4}$$

and $\left|\nabla^2 \mathrm{U}\right| \equiv \left[\partial^2 U_i/(\partial x_l \partial x_k)\;\partial^2 U_i/(\partial x_l \partial x_k)\right]^{1/2}$ representing the magnitude of the Laplacian operator applied to the underlying velocity field.

A key feature of the model — functioning effectively as a subscale model across the entire solution domain — is its ability to self-adapt to the turbulence scales contained within the unresolved subscale motion, in direct dynamic interplay with the underlying grid resolution. This adaptability facilitates the natural development of turbulent fluctuations. The characteristic length of the subscale structures is implicitly embedded within the solution of the transport equations. Unlike large

eddy simulation and other hybrid RANS/LES models, where grid spacing is a key modeling parameter, the present grid-spacing-free formulation does not rely on grid-dependent assumptions. The explicit independence of the model formulation from the grid spacing is particularly advantageous for highly non-uniform, anisotropic grid arrangements with an arbitrary cell topology. As a result, although the approach can formally be categorized within the hybrid LES/RANS framework, it is more accurately described as a time-accurate, sensitized RANS method. Consequently, the extent of the model's scale-resolving capability is inherently determined by the computed turbulence quantities associated with the residual motion. In contrast to the original SAS formulation, which used the von Kármán length scale L_{vK} ($L_{\mathrm{vK}} \propto \nabla \mathrm{U}/\nabla^2 \mathrm{U}$) as a trigger to activate the resolving mode, the current approach defines the triggering mechanism solely through the second derivative of velocity, as derived initially from the equation governing the integral length scale [20]. In line with the previously noted explicit independence of the turbulence model formulation from grid spacing, any residual dependence of the solution on the computational mesh is implicit and generally weaker, as demonstrated in prior studies (e.g. [21,22]). Moreover, the set of equations governing the evolution of the full residual stress tensor exhibits strong correlations among the various turbulent quantities, reflecting a high degree of internal coherence consistent with the underlying RANS methodology; it is recalled that the only difference between the baseline RANS-RSM formulation and its eddy-resolving extension is the inclusion of an additional production term in the transport equation for the inverse timescale, ω^h (Eq. (4)). Overall, this methodology for determining characteristic turbulence scales incorporates inherently an increased level of physical fidelity, which generally allows for the use of comparatively coarser grid resolutions without significant loss of accuracy.

For brevity, the full specification of the turbulence model are not reproduced here. Interested readers are referred to [18,23,24] for a comprehensive presentation of its structural properties and detailed model formulation. The model's predictive reliability has been extensively validated across a wide range of flow scenarios influenced by streamline curvature in configurations of varying physical and geometric complexity, including boundary-layer separation over sharp-edged and smoothly contoured surfaces, flows over transversely curved walls, and branch jet deflection in crossflow within T-shaped junctions; see e.g. [3,21,25–30].

3.2.1. Numerical method, solution domain, grid resolution

The eddy-resolving RANS model simulations are performed using the finite-volume-based, open-source toolbox OpenFOAM® (Open Source Field Operation and Manipulation), in which all relevant transport equations and supplementary functional relationships have been implemented. The Improved Instability-Sensitive Reynolds Stress Model (IISRSM) is applied within the time-accurate RANS framework [23], with a controlled, adaptive time-stepping strategy ensuring a Courant number consistently below one throughout the entire solution domain. Spatial discretization employs a second-order Central Differencing Scheme (CDS) for the convective terms of the momentum equations, while temporal derivatives are approximated using a second-order Backward Differencing Scheme (BDS). The implementation of the present near-wall formulation of the Reynolds stress equations (Eq. (2)) in the OpenFOAM® code builds upon on the high-Reynolds-number Reynolds stress model proposed by Gibson and Launder [31], which provides a bridge to the near-wall region. All additional terms and functions of the computational model — responsible for integrating the governing equations down to the wall and for modeling the effects of wall proximity on the mean flow and turbulence — are handled through corresponding numerical algorithmic implementations. In this context, the implementation of the stress dissipation correlation, ε_{ij}^h, is of particular importance, which is represented by a blended expression combining an anisotropic model term — consistent with near-wall asymptotic behavior — with a complementary off-wall isotropic formulation. The pressure–strain model term Φ_{ij} is implemented as a general multi-term expression of the form $f(a_{ij}, S_{ij}, W_{ij})$, as presented, for example, in [32]; the functional dependencies in the model coefficients ensure the vanishing of all Φ_{ij} components as the solid wall is approached.

The round jet entering the computational domain is generated through a separate simulation of a $L = 3D$ long pipe segment employing periodic inlet–outlet boundary conditions. The resulting fully-developed flow field is mapped directly onto the main-domain inlet. The computational domain retains a cylindrical geometry, bounded in the normal direction by the lower impingement wall and an upper bounding plate (see Fig. 4), and extending radially to $R = 12D$. The computational mesh is generated via OpenFOAM's blockMesh utility and refined through a comparative grid study, resulting in a fully hexahedral mesh. The radial domain extent is discretized with $N_r = 46400$ cells, while the normal (z) direction contains $N_z = 138$ cells, yielding a total of 6.4 million cells. Since the underlying sub-scale turbulence model is formulated for low Reynolds number, wall-resolved conditions, the required grid resolution must always be correspondingly fine. Consequently, mesh grading toward solid boundaries ensures that the first off-wall node lies well within the viscous sublayer, with a dimensionless wall distance z^+ significantly smaller than one (recall that the wall distance is normalized by the viscous length, $L_\nu = \nu/U_\tau$, where $U_\tau = \sqrt{\tau_w/\rho}$ denotes the local wall shear velocity). Accordingly, the wall-normal cell height across the entire domain ranges from $\Delta z^+ = 0.06$ in the immediate impingement region to $\Delta z^+ = 0.94$ near the outlet of the impingement channel. Such a high level of grid resolution near the wall is essential for accurately resolving the boundary layer under present highly non-equilibrium conditions, enabling precise evaluation of wall shear stress through the near-wall velocity gradient. The integration of the governing equation down to the wall, while accounting for the exact wall-boundary conditions based on the asymptotic behavior of turbulence quantities near the solid surface, is of decisive importance in the eddy-resolving RANS framework for accurately capturing their steep wall-proximity gradients. Radial resolution varies analogously, from $\Delta r^+ = 4.76$ at the jet center to $\Delta r^+ = 139.54$ at the configuration outlet. The sensitized RANS-RSM simulation using up to 96 processors required approximately 19 000 core hours per coupled simulation. This includes simulating the fully developed flow in the pipe-like nozzle and the impingement channel flow with up to 20 initial flow-through times and up to 90 subsequent flow-through times for time averaging.

3.3. Direct numerical simulations setup

Direct numerical simulations (DNS) are performed for the circular impinging jet configuration. The computational domain adopted in the DNS closely corresponds to that used in the eddy-resolving RANS approach, as shown in Fig. 4. Fully developed inflow boundary conditions are prescribed at the jet inlet section using a precursor simulation of a fully developed turbulent flow in a $L = 12D$ long pipe segment with periodic streamwise boundaries. To prevent entrainment of flow from the sides of the jet inlet section, a confinement plate, as practiced also in conjunction with the IISRSM simulations, is used. No slip boundary conditions are applied at the impingement plate for the velocity field, while at the lateral surfaces of the computational domain, the open boundary condition presented in [33] is imposed. The radial extent of the domain, measured from the impacting jet centerline, corresponds to $R = 10D$. The incompressible flow under consideration is free from external volume forces. Fluid properties are considered constant. The equations governing the instantaneous flow field are the Navier–Stokes equations:

$$\frac{\partial u_i}{\partial t} + u_j \frac{\partial u_i}{\partial x_j} + \frac{\partial p}{\partial x_i} - \frac{1}{\mathrm{Re}} \frac{\partial^2 u_i}{\partial x_j \partial x_j} = 0 \tag{5}$$

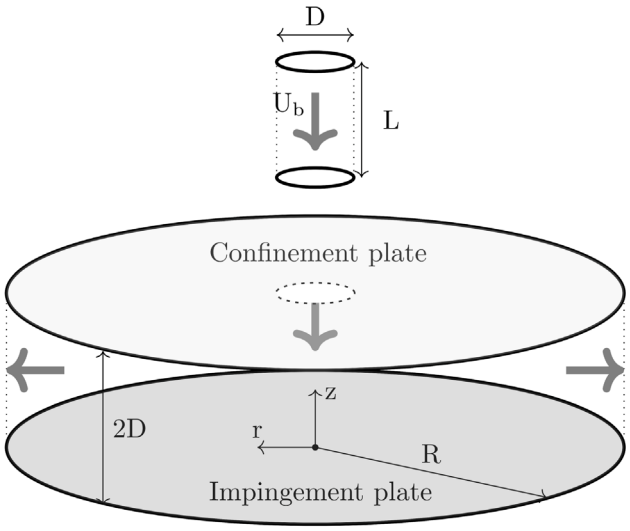

Fig. 4. Schematic representation of the solution domain for round-jet impingement adopted for the DNS and IISRSM simulations.

$$\frac{\partial u_i}{\partial x_i} = 0$$

where u_i $(i = 1, 2, 3)$ are the velocity components in the coordinate directions x_i $(i = 1, 2, 3)$, t is the time and p is the pressure field. Eq. (5) is made dimensionless using the bulk mean velocity U_b in the jet and the pipe diameter D. Consequently, the Reynolds number appearing in the equations is $Re = U_b D/\nu$, where ν is the kinematic viscosity of the fluid.

Eqs. (5) are integrated numerically using the flow solver Nek5000 [34]. The numerical code is based on the spectral element method (SEM) presented in [35] and is well-known for its very high-order spectral accuracy. In the SEM approach, the spatial discretization of the weak form of the governing equations is obtained by approximating the solution and test functions with Lagrange polynomials of degree N based on Gauss–Legendre-Lobatto (GLL) points. A $\mathbb{P}_N - \mathbb{P}_N$ formulation is adopted, in which the velocity and pressure spaces are approximated using polynomials of equal degree. The linear terms of the resulting space-discretized problem are advanced in time using a third-order backward differencing scheme, while non linear terms are advanced using the operator-integration-factor scheme [36].

In the framework of Nek5000, Eqs. (5) are numerically integrated using a Cartesian coordinate system, with the origin located at the intersection of the jet axis and the impingement plate. The x_3-axis coincides with the jet axis (z coordinate, Fig. 4) and is oriented to measure the distance from the wall, while the x_1- and x_2-axes lie on the plane of the impingement plate $(r, z = 0)$. The DNS computational mesh consists of $E = 2034995$ spectral elements, with the polynomial degree of $N = 7$ used to approximate the solution (for reference, the precursor pipe DNS employed 608175 spectral elements). The total number of degrees of freedom (DOF) in the computational grid is therefore $DOF = E(N + 1)^3 = 1041917440$ (for the precursor pipe flow simulation $DOF = 311385600$). The computational time required to obtain converged flow statistics in DNS amounts to approximately two million core hours (run on 16 384 cores). This includes the pipe flow simulation necessary to achieve fully developed pipe flow conditions at the nozzle outlet, as well as the initial flow field transients of the impinging jet, which are not included in the flow statistics. During post-processing, the solution and all statistical quantities accumulated during run-time are interpolated onto a cylindrical coordinates mesh whose coordinate system has the origin and z-axis coinciding with the original Cartesian coordinate system. Within the cylindrical coordinate system, r denotes radial locations, θ represents rotation, and z measures the distance from the impingement plate. The vector velocity field is denoted by the radial component u_r, the azimuthal component u_θ, and the axial component u_z.

4. Results and discussion

This section presents a selection of results from the comparative evaluation of the experimental and computational methodological approaches introduced earlier, focusing on the mean flow, the corresponding turbulent Reynolds stress correlations, as well as their anisotropic relationships and associated structural properties.

To provide an initial overview of the fundamental structural features of the flow configuration under consideration, Fig. 5 illustrates iso-contours of the mean velocity field together with those of the turbulence kinetic energy obtained from the DNS and IISRSM simulations, illustrating good qualitative and quantitative agreement. The snapshot of the IISRSM-related instantaneous velocity field is shown only to demonstrate the eddy-resolving capability of the model. The mean flow pattern displays the distinctive features of an impinging jet: a sharp velocity gradient variation beginning with prompt jet deceleration in the impingement zone, followed by a sudden 90-degree deflection that redirects the flow into the wall-jet region, where it undergoes rapid acceleration before gradually relaxing downstream. The visualization of the mean flow topology is intended to highlight the key flow regions within the impingement and wall-jet zones, providing a clearer basis for discussion. Mean streamlines traced from the inlet pipe reveal the structure around the stagnation region, where the incoming jet undergoes a right-angle bifurcation marked by strong curvature. This topological pattern reflects the rapid shift from flow deceleration during impingement to immediate acceleration downstream of the stagnation point $(r/D = 0.0)$. The deceleration of the vertical free jet and the subsequent acceleration of the horizontal wall-jet are directly linked to alternating pressure gradients in the stagnation zone. After impingement, the wall-jet spreads radially over the surface as streamlines are displaced and the near-wall flow widens, representing a process going along with gradual flow relaxation in the post-acceleration zone. In addition to the complex flow straining present in the vertical $r - z$ plane, the flow experiences transverse shear of varying intensity in the azimuthal direction, which decreases slightly with radial distance from the impingement center. Consequently, the circular redistribution of mass flow across the plate produces a relatively thin wall-jet layer that extends vertically up to $z/D \approx 0.3 - 0.5$ occupying not more than a quarter of the impingement channel height (recall that the point along a streamline in Fig. 5, corresponding to its extremum indicated by the strongest bending and coinciding with the zero gradient of the stream function, represents the location of zero velocity; this is also visible in Fig. 8); this is consistent with the previous argument that the upper confinement plate, which was not present in the experiment, does not noticeably influence the wall-jet flow. The dominant flow structures, composed of a vertically downward inflow and a wall-bounded jet, following the impingement region, interact with a surrounding low-intensity velocity field. Between the wall-jet and the upper wall, a weak backflow region emerges, as indicated by negative axial velocities in the velocity plots, signifying localized flow reversal.

The shear layer separating the high-velocity stream from the low-velocity region exhibits strong variability in its velocity gradients for both the free jet and the wall-confined jet. These steep gradients generate complex strain fields, which act as sources of enhanced turbulence, as clearly highlighted in the iso-contours of turbulence kinetic energy. Turbulence intensification is particularly pronounced in the near-impingement region $(r/D = 0.0 - 1.0)$, where it is driven by streamline curvature effects. This mechanism arises from the interaction of oppositely oriented spanwise (i.e., circumferential) vorticity components, which promotes an enhanced destabilizing effect on turbulence: a positive (anticlockwise) vorticity aligned with the global flow direction along a concavely deflected streamline in the flow

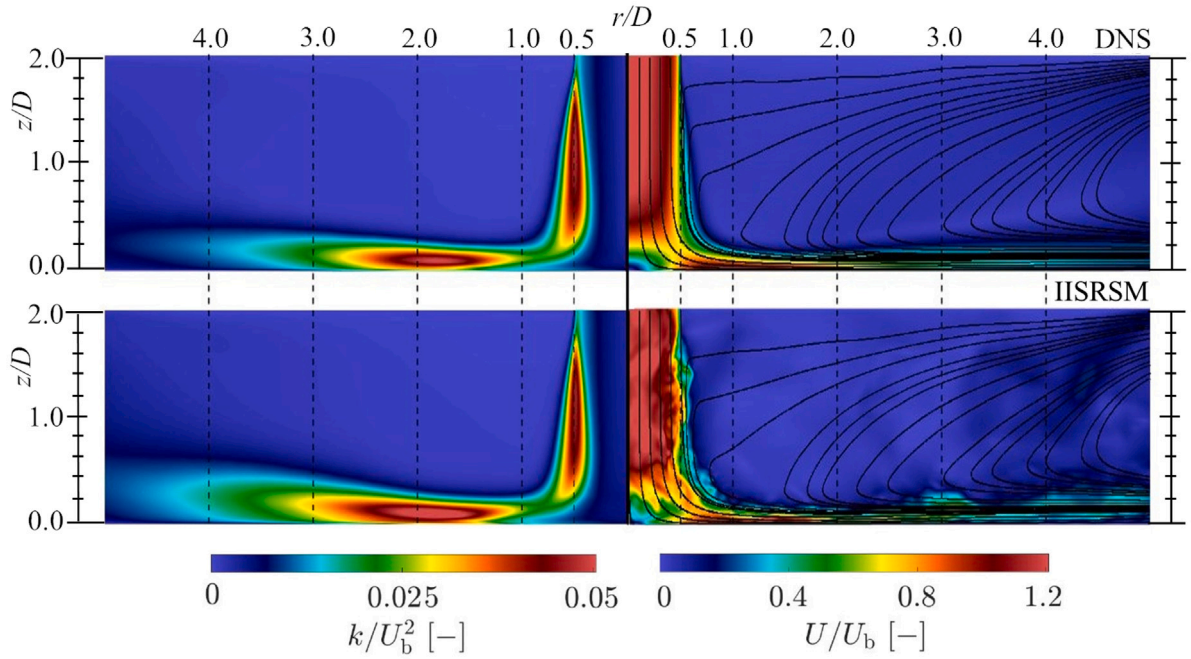

Fig. 5. Time-averaged DNS-related (upper) and instantaneous IISRSM-related (lower) isocontours of the velocity fields, along with their respective mean streamlines (right), and the corresponding time-averaged turbulence kinetic energy (left) in the central ($r-z$) vertical plane of the round-jet impingement configuration, as obtained from the DNS and IISRSM simulations.

stagnation zone ($\Omega_3\vec{e}_3 > 0$, where Ω_3 denotes the circumferential component of the angular velocity vector $\vec{\Omega}$, referred to as the system vorticity) and a negative, wall-bounded, mean shear-related vorticity ($\omega_3 = -0.5(\partial\overline{u}_r/\partial x_z)_{z=0} < 0$). The destabilizing effect of concavely progressing streamline curvature, manifested as an enhancement of turbulence intensity, was reported, for example, by Hoffmann et al. [37],Moser and Moin [38].

4.1. Free jet characteristics

The first quantitative comparison examines the development of the mean velocity profile of the downward free jet, normalized by the bulk velocity U_b, at various normalized distances from the nozzle exit ($z/D = 0.1, 0.2, 0.4$) measured from the coordinate origin at the center of the impingement plate, as well as very close to the nozzle exit ($z/D = 1.96$), see Fig. 6. The PIV experiments are shown as individual points, each corresponding to the measured velocity of a single pixel across all independent measurement series. This representation makes the low scatter of the measured values immediately apparent. For the mean axial velocities in Fig. 6, the data points are so densely clustered that they appear as a continuous band. The profile development clearly indicates the radial spreading of the free jet as it approaches the impingement plate. Overall, the PIV measurements and DNS results show close agreement across all vertical locations. The IISRSM results, however, display a somewhat flattened profile along the jet axis and slightly higher velocity values in the jet shear layer. This behavior is correlated with increased turbulent activity, which is further illustrated in the subsequent results sections.

The next step is the comparison of the corresponding Reynolds stress components $\overline{u_i'u_j'}$ at similar distances from the nozzle exit. The correlations $\overline{u_z'u_z'}$, $\overline{u_r'u_z'}$, and $\overline{u_r'u_r'}$, representing the velocity fluctuations in the axial (u_z') and radial (u_r') directions at $z/D = 1.96$ — immediately after the nozzle exit — are shown in Fig. 7, again normalized by the bulk velocity. These results closely match the fully developed pipe-flow characteristics, consistent with the inflow into the impingement channel domain. When comparing experimental and numerical results, good agreement is observed for the vertically and radially directed stress

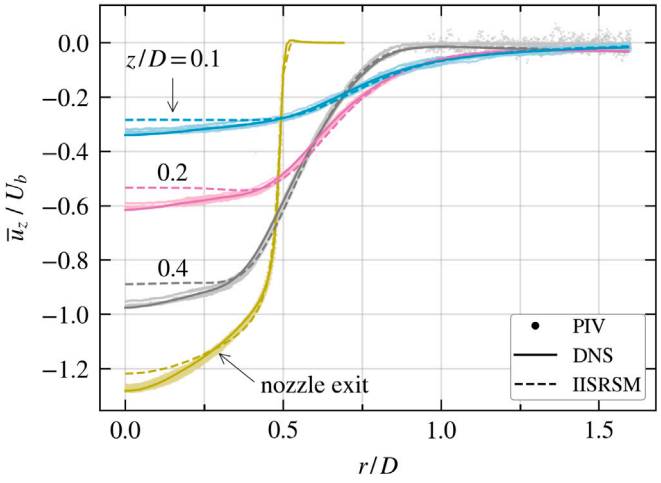

Fig. 6. Radial distribution of the mean velocity of the downward jet from the nozzle exit to the impingement plate.

components, $\overline{u_z'u_z'}$ and $\overline{u_r'u_r'}$, respectively, as well as for the shear stress component $\overline{u_r'u_z'}$. Slight deviations are notable in the IISRSM results, which show somewhat enhanced and shifted profile maxima toward the jet center. This behavior is associated with a correspondingly stronger velocity gradient in the shear layer of the exiting pipe-like nozzle jet.

As before, each experimental data point corresponds to the correlation obtained at a single image point. It is worth noting that the DNS data represent a lower bound for the normal stresses compared to the PIV measurements. This is most evident for $\overline{u_r'u_r'}$ and is expected if the DNS simulation is viewed as the 'noise-free' counterpart to the experiment, since any measurement noise can only increase the variances $\overline{u_z'u_z'}$ and $\overline{u_r'u_r'}$ relative to the noise-free case. For the cross-correlation term $\overline{u_r'u_z'}$, the situation is reversed: additional, independent noise in the individual components u_z' and u_r' weakens the correlation. Thus,

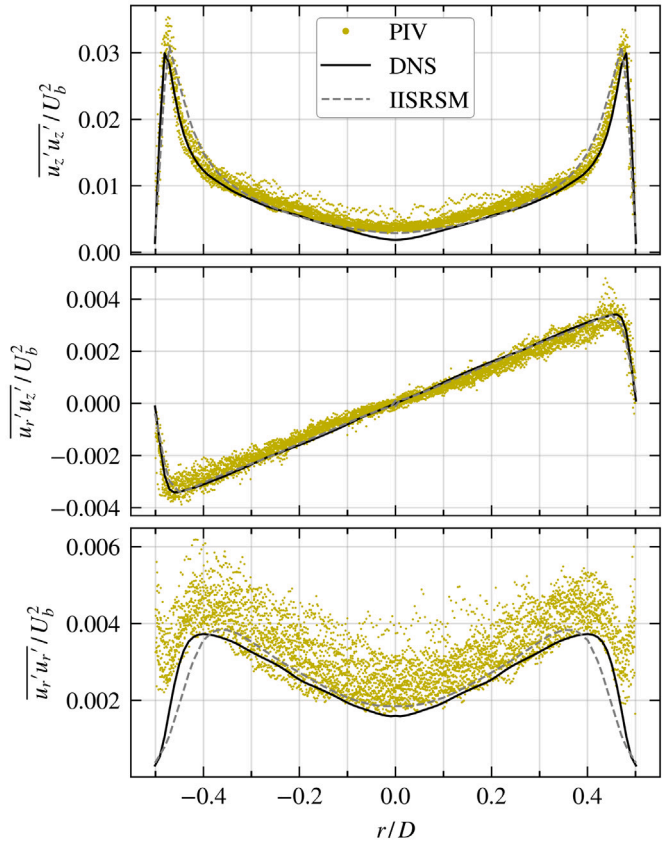

Fig. 7. Radial distribution of the Reynolds stress components close near the pipe exit ($z/D = 1.96$). Comparison between PIV measurements and simulation.

on average, the DNS results provide the upper bound (in magnitude) of the PIV data, which is exactly what the experiment shows. At the nozzle outlet, where artifacts due to out-of-plane tracer-particle motion are not expected, two conclusions follow: (1) the experimental data are limited only by statistical noise, with no systematic errors biasing the derived mean flow fields and Reynolds stress components, and (2) the experimental setup provides inlet conditions that closely resemble fully-developed turbulent flow, thereby enabling a reliable near-wall comparison between experiment and simulation.

4.2. Impingement channel: velocity and Reynolds stress profile developments

To provide quantitative support for the experimental and computational findings, profiles of the mean flow and associated turbulence variables are directly compared at selected cross-sections. The evaluation locations, marked by dashed lines in Fig. 5, span three characteristic flow regions: the immediate impingement zone ($r/D = 0.5$), the transition region characterized by alternating velocity gradients and wall-jet formation ($r/D = 1.0$), and the developing wall-jet region ($r/D = 2.0$, 3.0, 4.0). The flow quantities analyzed include the radial (streamwise) velocity component ($\overline{u}_r$; Fig. 8), the distribution of wall shear stress along the bottom wall (Fig. 9), and the streamwise ($\overline{u_r'u_r'}$), wall-normal ($\overline{u_z'u_z'}$), and shear ($\overline{u_r'u_z'}$) Reynolds stress components (Fig. 10), all appropriately normalized by the bulk velocity of the inflow pipe (U_b).

4.2.1. Velocity profile development

Fig. 8 shows the evolution of the mean velocity ($\overline{u}_r$) profiles in the radial direction of the outflowing impingement channel. The dimensionless wall-normal coordinate z/D is plotted on a logarithmic scale to magnify the immediate wall vicinity region and enable a closer look into the near-wall behavior.

The profiles reveal an intensification of flow momentum during impingement, as evidenced by flow acceleration ($r/D = 0.5$–1.0), followed by a transition to the wall jet ($r/D \geq 1.0$) and a subsequent momentum weakening. As noted earlier, the axial velocity profiles in the upper part of the flow field — outside the free-jet and wall-jet regions (blue-shaded area in Fig. 5-right) — exhibit very low negative values, indicating weak flow reversal. The velocity plots demonstrate very good overall agreement between the present experimental and computational results regarding the shape of the profiles, in terms of their maxima and corresponding wall distances. While the DNS data match the measurements almost exactly, the modeled results exhibit some deviations from the experimental reference. In particular, the development of the wall jet region in terms of spreading intensity — characterized by slightly lower velocity maxima at a somewhat greater wall distance and correspondingly lower velocity values in the immediate wall vicinity, in accordance with the continuity conditions — appears distinctly different. Nevertheless, the model correctly predicts the extent of the upper-wall-related recirculation zone, as confirmed by the position of the velocity profiles intersection with the zero line. Since the mean flow intensity governs turbulent transport dynamics — controlling momentum exchange and, in turn, the size of the reversal region — its reduction in the backflow zone corresponds to weak turbulence activity, as also evident in Fig. 10. The velocity profiles furthermore reveal strong gradients in both wall-normal and wall-parallel directions, reflecting variable acceleration intensities within the developing wall jet. The strongest relative acceleration, associated with the maximum wall shear stress and the steepest near-wall velocity gradient occurring at $r/D = 0.5 - 1.0$, is subsequently followed by a rapid global flow deceleration within the region $1 < r/D \leq 2$. At the same time, this implies a thickening of the wall jet, characterized by an increased velocity gradient within its shear layer, which contributes to enhanced turbulence production, as reflected in the correspondingly amplified Reynolds-stress components at $r/D = 2.0$ (see Fig. 10); this is especially pronounced with respect to the impingement wall-parallel stress component $\overline{u_r'u_r'}$. Subsequently, the flow deceleration proceeds monotonically, accompanied by a slight weakening of the mean velocity gradient and a corresponding decrease in turbulence intensity. These features are in a close mutual agreement among all three result sets. The discrepancies in the modeled results are primarily confined to the very near-wall region ($z/D < 0.1$), where velocity amplitudes differ slightly from experimental data, although the associated wall-normal gradients remain well captured. This consistency is reflected in the distribution of wall shear stress at the bottom wall (Fig. 9).

4.2.2. Wall shear stress distribution

Fig. 9 shows the non-dimensionalized wall shear stress $(D/U_b)(d\overline{u}_r/dz)$ over the dimensionless radius, r/D, of the impingement plate at $z = 0$. For the PIV measurements, the wall shear stress is computed from the slope of the mean radial velocity profiles at the wall (see Fig. 8). The latter is estimated using a polynomial fit of the radial velocity profile close to the wall, which is forced to be zero at the position of the wall. Error bars represent the 3σ-standard deviation of the fit coefficient. The computational results were obtained by directly calculating the velocity gradient between the velocity value of the grid cell closest to the wall and the zero wall velocity enforced by the no-slip boundary condition at the wall surface. For both computational methods, the cell closest to the wall is well within the viscous sublayer at $z^+ = zu_\tau/\nu < 1$, allowing the use of a simple difference quotient to approximate the wall shear stress.

The variation in the friction coefficient along the bottom impingement wall directly corresponds to the development of velocity profiles. The wall shear stress distribution exhibits a sharply pronounced peak near the stagnation point at the impingement center at $r/D \approx 0.8$,

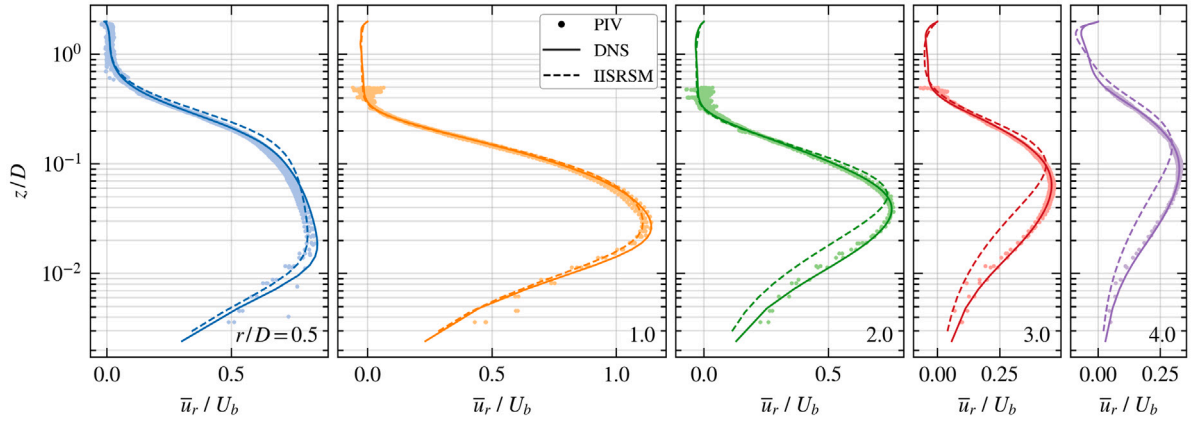

Fig. 8. Wall-normal profiles of the mean radial velocity $\overline{u}_r/U_b$ close to the wall and at different radial positions $r/D = 0.5, 1, 2, 3 \& 4$; the location $r/D = 0.5$ corresponds to the nozzle exit. The wall-normal coordinate is plotted on a logarithmic scale to magnify the relevant near-wall region.

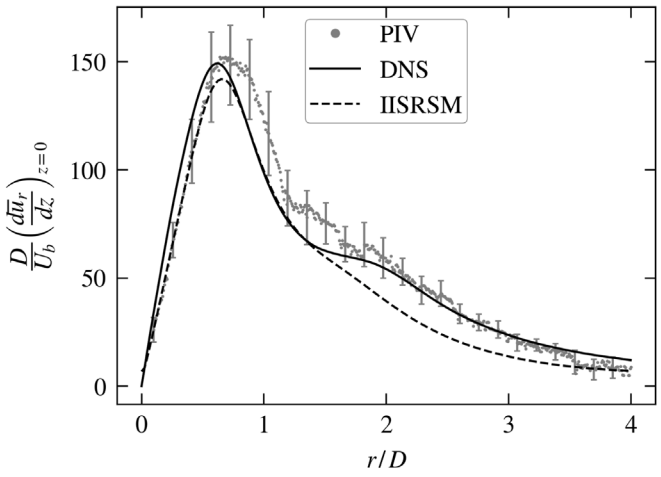

Fig. 9. Dimensionless wall shear stress as a function of the radial position. Error bars correspond to the 3σ standard deviation from extrapolation of the experimental velocity profiles to the wall surface.

followed by a continuous, monotonic decay throughout the downstream wall-jet region. This peak clearly arises from the abrupt local flow acceleration at the transition toward the wall-jet regime, which is directly visible in the velocity profiles at radial locations between $r/D = 0.5$ and $r/D = 1.0$, Fig. 8 (clearly observable in Fig. 5-right). The wall shear stress distribution follows a trend consistently reproduced in both experiments and computations. A notable deviation occurs, however, where the IISRSM fails to capture the distinctive plateau-like behavior observed at a dimensionless distance of $r/D \approx 2$ from the stagnation point. This trend in the wall shear stress distribution is directly linked to the well-documented secondary maximum in the Nusselt number distribution, which represents a feature that is not currently addressed but has been firmly established in prior studies as originating from the reorientation of fluctuating velocity components at this precise location, as discussed in [4]. Considering that IISRSM is designed to resolve spectral dynamics through turbulence transport equations at a level of detail corresponding to a given spatial resolution, the evidence suggests that the current numerical grid may not be sufficiently fine at this specific locality to accurately resolve the wall-proximity related secondary flow structures.

4.2.3. Reynolds stress profile developments

Fig. 10 presents the profiles of the Reynolds stress components $\overline{u'_z u'_z}$, $\overline{u'_r u'_r}$, and $\overline{u'_r u'_z}$ at the same radial positions, normalized appropriately by the inlet bulk velocity U_b. The wall-normal coordinate z/D is shown on a logarithmic scale to highlight near-wall behavior.

The agreement between PIV (dots) and DNS (solid lines) results is very good at all radial positions, both in terms of shape and magnitude of the stress components. Nevertheless, in contrast to the nozzle exit (Fig. 7), there are very small systematic deviations that are not simply due to statistical noise. For instance, the DNS is no longer the lower bound for the normal stresses $\overline{u'_z u'_z}$ and $\overline{u'_r u'_r}$ from the PIV, as it was the case at the nozzle exit. Near the wall, cross-correlation of PIV images is more prone to artifacts, as e.g., due to particles moving out of the laser sheet between images (out-of-plane motion), lower tracer particle density, small imperfections in wall alignment, or partial shadowing of scattered light from the particles by the wall. The latter is partially compensated by the Scheimpflug alignment of the camera with respect to the laser light sheet. These uncertainties are not statistical and are only partly reflected by the larger scatter of the experimental data points compared to those at the nozzle outlet. It is widely recognized that standard cross-correlation PIV techniques may introduce spurious velocity fluctuations and consequently overestimate turbulence intensities in the near-wall region, due to their limited ability to resolve small-scale motions close to the wall (see, e.g., [39,40]). Considering these uncertainties, however, the agreement with the DNS simulation can be considered as very close. Overall, the IISRSM predictions demonstrate good agreement with experimental and DNS data, in terms of both profile shape and magnitude, across nearly all radial locations. A notable discrepancy lies in the excessively amplified radial stress component ($\overline{u'_r u'_r}$) parallel to the impinging plate within the wall-jet development region as distance from the immediate impingement area increases ($r/D \geq 2$). This is consistent with a correspondingly higher spreading rate of the wall jet layer in the IISRSM simulations, as already observed for the radial velocity profiles in Fig. 8.

At $r/D = 0.5$, corresponding to the immediate pipe exit, the peak intensities of all stress components clearly stem from the near-wall turbulence within the inflow pipe itself. Moving downstream, the Reynolds stress evolution reveals a sharp increase in turbulence production triggered at and beyond the pipe edge, where a free shear layer rapidly forms between the jet core and the surrounding low-velocity fluid. Accordingly, the immediate impingement region and the shear layer zone, aligned with the streamline separating the wall-bounded jet from the low-velocity flow region, acts as a hotspot of turbulence amplification, with all stress components attaining their maxima precisely at this wall distance across all radial locations. This behavior reflects the destabilizing effect of streamwise curvature-driven turbulence production, directly tied to the directional misalignment between global and local spanwise (azimuthal) vorticities. Within the horizontal, radially expanding channel, all Reynolds stress components

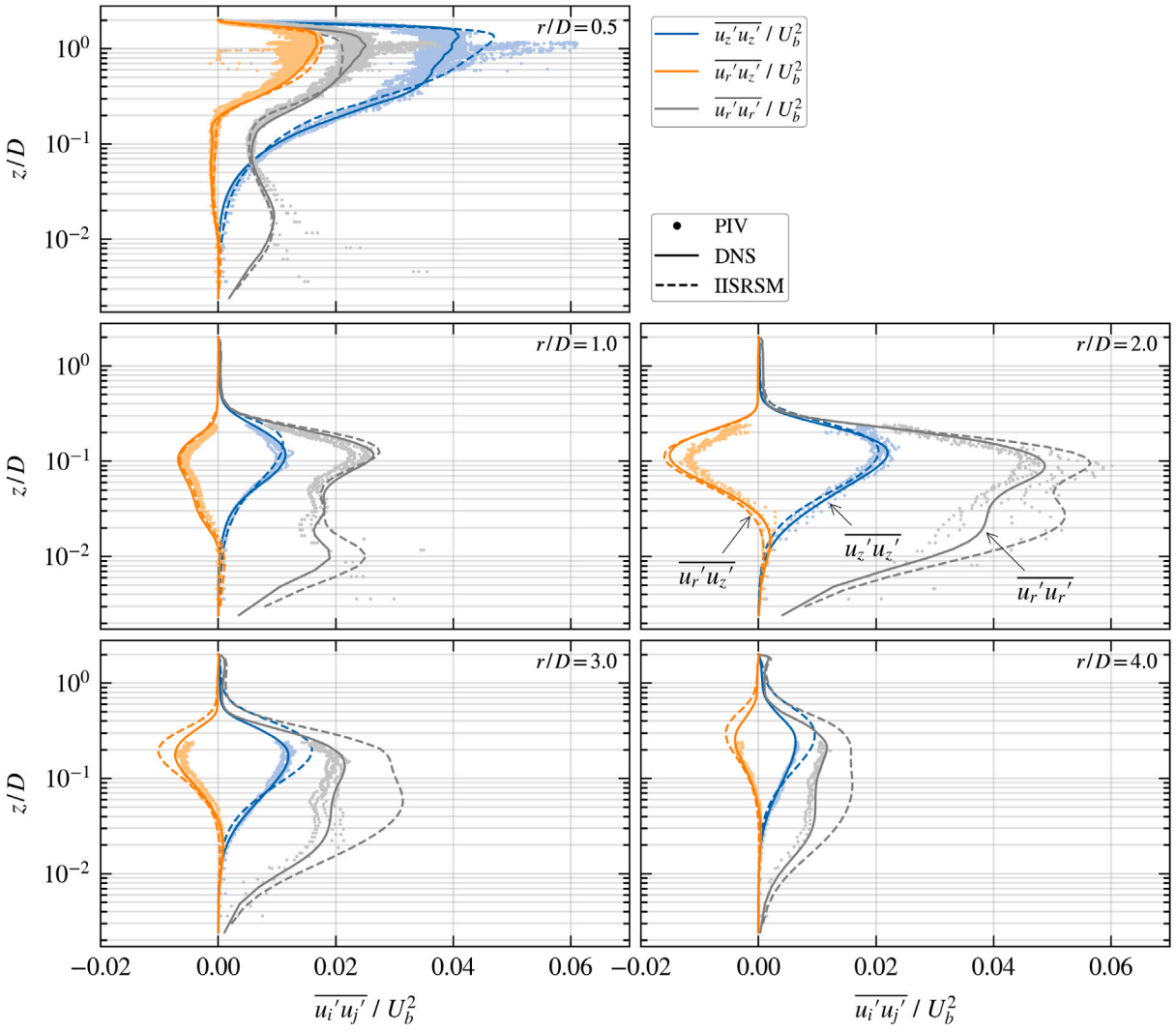

Fig. 10. Wall-normal profiles of the normalized Reynolds stress components $\overline{u_i'u_j'}/U_b^2$ close to the wall and at different radial positions $r/D = 0.5, 1, 2, 3 \& 4$; the location $r/D = 0.5$ corresponds to the nozzle exit. The wall normal coordinate is plotted on a logarithmic scale to highlight the area near the wall.

progressively intensify, reaching their peak turbulence levels at approximately $r/D = 2.0$. This location is marked by a localized steepening of the velocity gradient near the free wall-jet boundary and across the associated shear layer (see Fig. 8). Beyond this point, the turbulence intensity gradually relaxes as the flow approaches the outlet.

As the flow bends 90° from a downward free jet into a radially expanding wall jet, the stress tensor components undergo a fundamental redistribution: the free-jet streamwise stress component $\overline{u_z'u_z'}$ transforms into the wall-normal stress component at impingement, while the free-jet normal stress reorients into the radial component $\overline{u_r'u_r'}$ along the wall-parallel wall jet. This transformation is clearly demonstrated by the significant decrease in the value of $\overline{u_z'u_z'}$ from a high near-outlet maximum ($z/D \approx 1.96$, $r/D = 0.5$) down to a near-wall peak of very small magnitude at $z/D \approx 0.02$. This strong attenuation is a direct signature of the wall-induced kinematic wall blockage effect and is correctly reproduced by all methodologies applied. Within the wall jet itself, the $\overline{u_r'u_r'}$ profile exhibits a characteristic double-maximum structure: a near-wall peak at $z/D \approx 0.03$ driven by intense wall shear, and an off-wall peak at $z/D \approx 0.3$ coinciding with the wall-jet-related shear layer, characterized by a high velocity gradient. This dual behavior, clearly observed for $0.5 \leq r/D \leq 2.0$, is accurately captured across methods. Beyond $r/D \geq 2.0$, however, the off-wall maximum consistently dominates over the near-wall one, underscoring the shifting turbulence dynamics in the outer wall-jet region.

In the wall-jet region, $\overline{u_r'u_r'}$ represents the streamwise stress component and contributes predominantly to the turbulent kinetic energy (cf. Fig. 5-left). The significant increase in the magnitude of the radial turbulent stress component $\overline{u_r'u_r'}$ at $r/D = 2.0$, relative to its value at $r/D = 1.0$, can be understood by analytically examining the corresponding production rate: $P_{rr} \rightarrow -\overline{u_r'u_r'}\,\partial U_r/\partial r - \overline{u_r'u_z'}\,\partial U_r/\partial z$. In this region, both $\overline{u_r'u_r'}$ and the wall-normal velocity gradient $\partial U_r/\partial z$ are positive, whereas the shear stress $\overline{u_r'u_z'}$ is consistently negative, as is the radial velocity gradient $\partial U_r/\partial r$ between $r/D = 1.0$ and 2.0. As a result, all terms in the production expression are positive, leading to an increased production rate P_{rr}.

Finally, it must be emphasized that, in impinging jet configurations, particularly in the wall jet zone, the wall-normal stress component, $\overline{u_z'u_z'}$, is crucial for turbulence models that use gradient diffusion hypothesis-based closures for turbulent heat fluxes, as it appears in

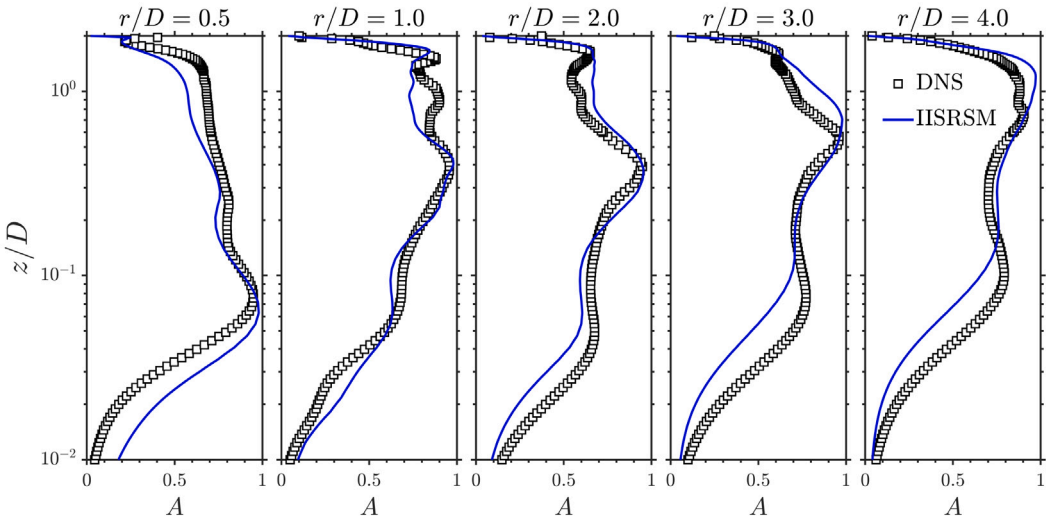

Fig. 11. Profile development of the two-component anisotropy parameter A within the impingement channel, as obtained by DNS and IISRSM. The wall normal coordinate is plotted on a logarithmic scale to highlight the area near the bottom wall.

the corresponding model coefficient. Its correct prediction is a decisive prerequisite for faithfully representing convective heat transfer. The characteristic sign reversal of the shear stress component $\overline{u_r' u_z'}$ is captured with high fidelity, both in terms of the precise location of the change and the associated magnitude. This reversal is a direct consequence of the intense local streamline curvature, which acts in a strongly destabilizing fashion and drives a marked amplification of turbulence levels. At the same time, it must be emphasized that the dominant mechanism shaping the overall topology of the mean velocity field is not the Reynolds stress gradient, but the mean pressure gradient. The latter exerts overwhelming control in the momentum balance within the impingement region, decisively surpassing the influence of Reynolds stress variations and governing the global flow topology.

5. Reynolds stress anisotropy

This section focuses on representing the characteristic states of turbulence in terms of their anisotropic properties. The relevant analysis is conducted with reference to the results presented in Figs. 12–14. Specifically, the section evaluates the variation of the Reynolds stress anisotropy tensor, $a_{ij} = \overline{u_i' u_j'}/k - 2\delta_{ij}/3$, along with the corresponding second and third invariants, $-II_a = a_{ij}a_{ji}/8 = A_2/8$ and $III_a = a_{ij}a_{jk}a_{ki}/24 = A_3/24$, and the two-componentality parameter, $A = 1 - 9(A_2 - A_3)/8$; it is recalled that the two-component anisotropy parameter A takes the value 1 for strict turbulence isotropy and the value 0 for the strongest level of anisotropy (the profiles of the A parameter across the impingement channel and its entire field are illustrated in Fig. 11 and Fig. 13-left). These quantities are obtained from the three-dimensional flow fields computed by DNS and IISRSM, following the framework of Lumley and Newman [8] and Choi and Lumley [41]. Since the circumferential Reynolds stress component $(\overline{u_\theta' u_\theta'})$ was not measured in the 2D PIV experiments, its contribution to the turbulence anisotropy analysis cannot be included in the present interpretation. Nevertheless, a comparative assessment of all three methodologies has been carried out by considering only the Reynolds stress anisotropy components active in the vertical r–z plane, namely a_{rr}, a_{zz}, and a_{rz} (with $a_{\theta\theta} = 0$ and $a_{rr} + a_{zz} = 0$, due to the zero trace of the 2D tensor). As shown in the Appendix, this comparison demonstrates a high degree of agreement (cf. Fig. A.15).

In addition, the functional dependency between the second and third invariants of the Reynolds stress anisotropy can be conveniently represented on an anisotropy invariant map, which forms a triangular domain in the invariant $(III_a, -II_a)$ space (Fig. 12-upper). Its corner points correspond to three limiting turbulence states: three-component isotropic ($3C$ or X_{3C}), two-component isotropic ($2C$ or X_{2C}), and one-component ($1C$ or X_{1C}) limits. The triangle edges represent the associated limiting processes — axisymmetric contraction ($3C \rightarrow 2C$), axisymmetric expansion ($3C \rightarrow 1C$), and two-component anisotropic turbulence ($2C \rightarrow 1C$). The three-component isotropic state ($3C$) exactly complies with the two-component parameter value $A = 1$, and the value of $A = 0$ typically characterizes the flow areas immediately adjacent to the solid wall, represented by the turbulence states connecting the $2C$ and $1C$ vertices. An alternative but equivalent representation is the barycentric map (Fig. 12-lower), introduced by Banerjee et al. [9] (see also [10]), which is constructed from the ordered eigenvalues $(\lambda_1 \geq \lambda_2 \geq \lambda_3)$, arising from the diagonalization of the anisotropy tensor a_{ij}. These eigenvalues quantify the relative weighting of velocity fluctuation correlations, analogous to the invariants $-II_a$ and III_a, thereby defining the turbulence componentality. The vertices of the barycentric triangle, $X_{1C} = (0, 1)$, $X_{2C} = (0, 0)$, $X_{3C} = (1/2, \sqrt{3}/2)$, and the connecting edges represent the same limiting states as in Lumley's map, but here each boundary state is assigned equal weight. The invariant coordinates $(III_a, -II_a)$ are accordingly projected onto the barycentric coordinates (x_B, y_B), defined as functions of the eigenvalues λ_i. It is important to emphasize that all realizable turbulence states are confined within these triangular domains and along their boundaries. Both evaluation tools for representing Reynolds stress anisotropy — Lumley's anisotropic map and the equilateral barycentric map — offer distinct advantages. The nonlinear triangular domain of Lumley's map allows turbulence states to be conveniently quantified in direct dependence on the second and third anisotropy invariants. Complementary to this, the linear barycentric domain facilitates an additional application of the underlying analytical rationale, as the barycentric coordinates (x_B, y_B) can be used to directly remap the anisotropic turbulent states onto the actual physical flow domain, as shown in Fig. 13-right. The following discussion will refer simultaneously to all turbulence anisotropy-related results shown in Figs. 12–14.

The turbulent states within the central region of the free jet, the immediate impingement zone, and most of the outflowing impingement

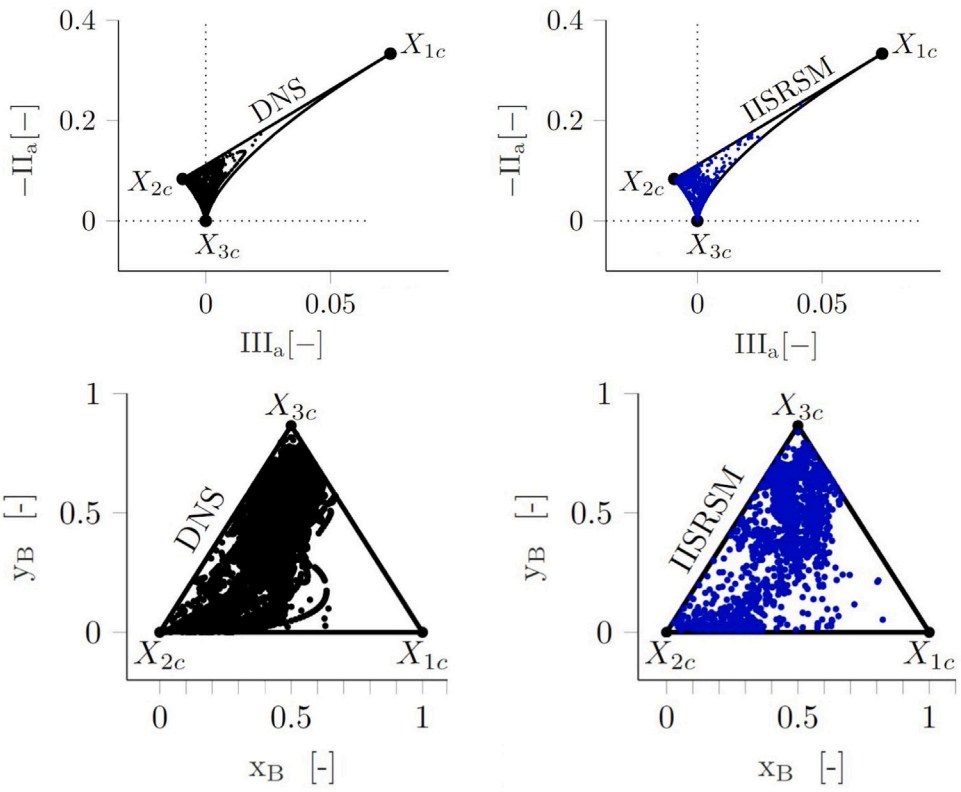

Fig. 12. The Lumley's anisotropy map with second II_a and third III_a anisotropy invariants (upper; note that $-II_a$ is merely a notation; the second invariant itself cannot take negative values) and the corresponding barycentric turbulence anisotropy map (lower), as obtained by DNS and IISRSM.

channel — particularly the regions bordering the free and the wall jets — are characterized by a weak anisotropy, as evidenced by the correspondingly high values of the two-component parameter A. Throughout most of the flow domain, the parameter A, which serves as a measure of the anisotropy level of the underlying Reynolds stress field, attains values of 0.7 or higher (see Figs. 11 and 13-left), clearly indicating a low degree of anisotropy. This observation is consistent with the globally present adverse pressure-gradient effects typically associated with impinging jet configurations, where the free jet undergoes strong deceleration upon impact, complying with a strongly curved local mean flow within the resulting stagnation zone. This finding is further supported by interpreting the characteristic states of turbulence in terms of both the functional dependence between the second and third invariants within Lumley's invariant map and the barycentric coordinates in the associated equilateral triangular space, as shown in Fig. 12. Each individual point in the two corresponding anisotropy domain spaces represents the computational result referring to all grid cells in the flow domain. As expected, the general realizability of the turbulent structure predicted by both computational approaches is fulfilled without exception, with all results lying within the interiors of the triangles. This interpretation also provides a clear identification of the overall turbulence states in terms of their anisotropic properties. Accordingly, both DNS- and IISRSM-based results are primarily bounded by the $3C$ (X_{3C}) and $2C$ (X_{2C}) isotropic states, indicating that the turbulence state existing in the largest portion of the flow domain is characterized by negative values of the third anisotropy invariant III_a; these states lie predominantly between the left boundary of the invariant triangle (spanning the $3C$ and $2C$ states), which corresponds to the previously introduced axisymmetric contraction process of turbulent structuring, and the turbulent state defined by ($III_a = 0, -II_a$), denoting the so called plane-strain event of turbulence.

By utilizing the properties of the barycentric anisotropy map in Fig. 12 and transferring its information back into the physical domain through color-coding of the turbulent states, the isocontours generated in Fig. 13-right (the color-coded barycentric triangle shown enables exact assignment of a specific color to a corresponding turbulent state) provide improved insight into the anisotropic turbulent state of the round jet impingement. When directly comparing the images of the two-component parameter A (Fig. 13-left) and the color-coded barycentric coordinate fields in Fig. 13-right, it is important to note that the values within the fields of the two-component parameter A align perfectly with the color coding of the barycentric field diagrams. For example, the dark red regions labeled $A \approx 1$ in 13-left coincide exactly with the corresponding dark blue regions in 13-right, demonstrating that both approaches for the anisotropy characterization reliably identify areas of three-component isotropic turbulence ($3C$). Accordingly, the close-to-unity values of the A-parameter fields obtained by DNS and IISRSM are strongly concentrated in the narrow regions of the shear layers bounding the free jet and the wall jet with the immediate surroundings, characterized by the highest turbulence production, which coincide precisely with the maxima of turbulence intensities (cf. Fig. 10). The enhancement of turbulence production, generally correlated with a significant weakening of anisotropy, is also closely related to flow stagnation and the subsequent effects of streamline curvature.

Towards the lower and upper impingement channel walls, the A values exhibit a continuous decrease, indicating correspondingly strengthen anisotropy. This behavior is evident in the blue regions of the A-parameter field (note also the tendency of the A profiles

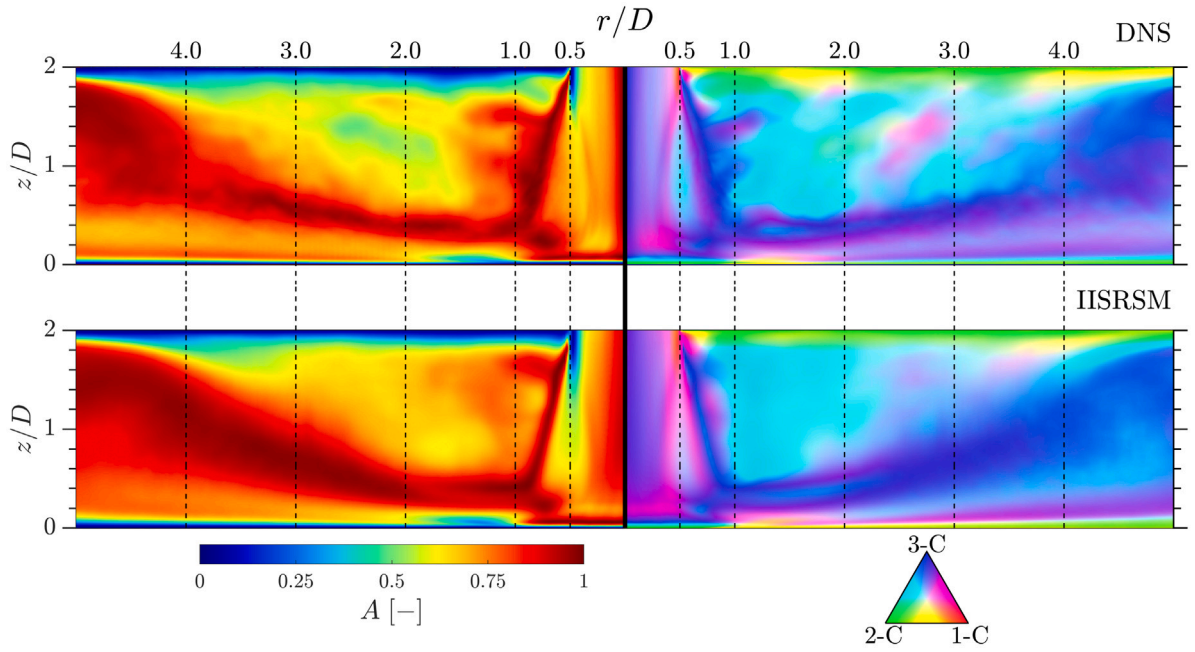

Fig. 13. Fields of the two-component anisotropy parameter A (left) and the barycentric turbulence coloring (right), illustrating different turbulence states bounded between the three-component isotropic (3C), two-component isotropic (2C), and one-component (1C) limits, as obtained by DNS and IISRSM.

to decrease toward zero at the walls in Fig. 11), as well as in the corresponding yellow-to-green regions at both the impingement wall and the upper confinement wall in the barycentric coordinate field (Fig. 13-right). These regions denote the turbulence state bounded by the transition from the yellow segment of the barycentric triangle (see the barycentric triangle in Fig. 13-right), which occurs immediately after the $1C$ limit toward the green-colored two-component isotropic limit ($2C$). Regarding the latter, it is instructive to examine the very narrow (blue-colored) area immediately outside the pipe ($z/D = 2$, $r/D = 0.5$). It is well known that the turbulence state in the core region of fully-developed pipe flow corresponds to very weak anisotropy, with $A \approx 1$, whereas the highest level of anisotropy occurs in the immediate vicinity of the wall; the wall itself is characterized by $A = 0$. This narrow region of high anisotropy undergoes a rapid transition to a weakly anisotropic state in the area immediately above the free-jet shear layer. Furthermore, it is noteworthy to analyze the flow conditions at the jet's immediate impact location ($z/D \to 0$, $r/D = 0$). At this location, the A values obtained from DNS and IIS-RSM exceed 0.9 (see Fig. 13-left, as well as Fig. 11; in particular the A profile at the radial location $r/D = 0.5$ reaches values ≥ 0.9 at the wall-normal distance of $z/D = 0.07$). This corresponds to a turbulence state resembling the axisymmetric contraction found between $3C$ and $2C$ (light-blue area at the impact point, for $z/D \approx 0.05 - 0.07$ and $r/D = 0.0 - 0.9$ in Fig. 13-right). The turbulent state in the region outside the free and wall jets is likewise dominated by axisymmetric contraction ($3C$-$2C$), characterized by negative values of the third anisotropy invariant (dark-to-light blue regions in Fig. 13-right). In these regions, A parameter exceeds approximately 0.75, corresponding to the red areas in Fig. 13-left, which in turn precede the yellow regions where $A \approx 0.6$. These zones, spanning $z/D \approx 0.3$–2.0 and $r/D = 1.0$–4.0, are characterized by low momentum transport (see the velocity profiles in Fig. 8, which exhibit small negative values) and, consequently, very low turbulence intensities, with the Reynolds stress components following each other closely at this uniformly low level (see Fig. 10); note that a logarithmic scaling of the wall coordinate is used in both figures.

Fig. 14 illustrates the trajectories of the Reynolds stress anisotropy in an equilateral barycentric anisotropy map at locations ranging from the immediate impact region ($r/D = 0.5$) to the far-wall jet region ($r/D = 4.0$). The trajectories originate at the bottom impingement wall ($z/D = 0$), represented by the horizontal line connecting the X_{2C} and X_{1C} map corners, which characterizes two-component anisotropic turbulence, and extend over the entire cross-sectional extent up to the upper confinement wall ($z/D = 2$).

In the immediate impingement region at $r/D = 0.5$, which is affected by the simultaneous action of complex flow straining underlying the strong, right-angled flow skewing, the turbulence state lies close to the X_{2C}-related state (i.e., on the transition from $2C$ to $3C$, between the green-coded and light-to-dark blue segments of the barycentric triangle). This indicates a steep increase from the strongest anisotropy level, corresponding to $A \approx 0$ at the wall itself ($z/D = 0.0$), to a near-unity value of the two-component parameter A at $z/D \approx 0.07 - 0.08$, which denotes a strict isotropic state (see also the corresponding A profile in Fig. 11). As the trajectory moves away from the wall, it progresses almost parallel to the $2C \to 3C$ map boundary, associated with negative III_a values (recall that the so-called plane strain state of turbulence is denoted by $III_a = 0$, as indicated by the red dashed line in the barycentric triangle). The sparsely distributed data points forming the trajectory progression toward the $3C$ limit correspond to the thin near-wall region extending to the end of the downward jet shear layer at $z/D \approx 0.1 - 0.2$ (see also Fig. 5). This narrow region is indicated by consecutively arranged green, light blue, and dark blue stripes in the immediate impingement area at $r/D = 0.5$ in Fig. 13-right, with the dark blue stripe corresponding to the dark-red stripe in the A-parameter field in Fig. 13-left, denoting the flow structure underlying the isotropic state of turbulence with $A \approx 1$. The region immediately adjacent to the impingement wall within the central impact zone is subject to the combined influences of wall proximity, flow stagnation, and the destabilizing effect of streamline curvature. All these phenomena contribute, to varying degrees, to the intensification of turbulence, which begins at $z/D \approx 0.1$, consistent with the minimum in the $\overline{u_r' u_r'}$

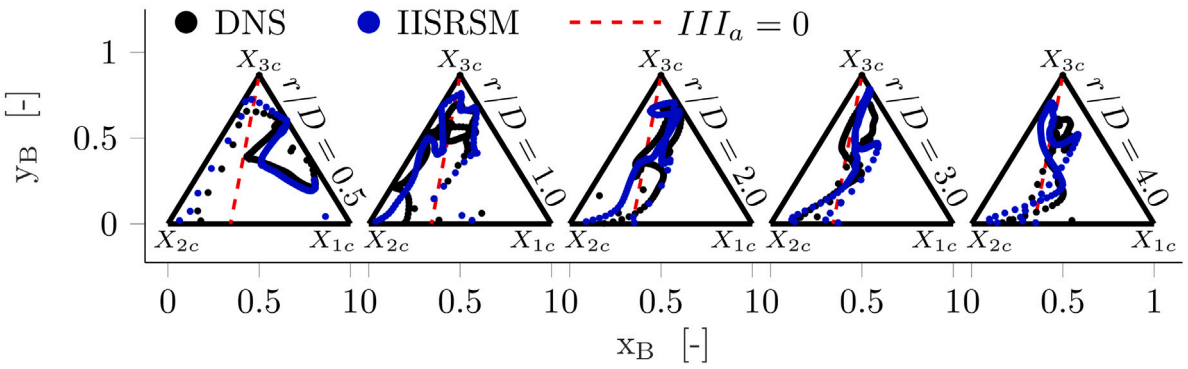

Fig. 14. Reynolds stress anisotropy trajectories within the barycentric turbulence anisotropy map at five selected positions in the impingement channel, as obtained by DNS and IISRSM; the red dashed line denotes the so called plane-strain state of turbulence with $III_a = 0$.

profile and reaches its highest value at $z/D \approx 0.015$ (see the formation of the wall-related turbulence intensity maximum in the $\overline{u_r' u_r'}$ profile in Fig. 10). As the distance from the wall increases, the trajectory crosses the free-jet shear layer at a wall distance of $z/D \approx 0.1$, a region characterized by the strongest streamline curvature (cf. Fig. 5), corresponding to the magenta-colored region in the barycentric coordinate field. Accordingly, the trajectory deviates from the $2C \rightarrow 3C$ map edge and bends toward the map boundary between $3C$ and $1C$, which is associated with positive III_a values. In this region, the otherwise weak anisotropy slightly strengthens with distance from the impingement wall, entering the shear layer of the free jet at $z/D \approx 0.3 - 0.4$. The magenta color-coding in the barycentric coordinate field corresponds to the red–yellow region along the ordinate $r/D = 0.5$ in the A-parameter field up to $z/D \approx 0.3 - 0.4$, with A taking the values between $0.6 - 0.7$. Subsequently, the trajectory point marking the sharp, right-angled change in trend — from the map boundary $3C \rightarrow 1C$ toward the center of the barycentric triangle — corresponds to a light-blue region denoting the DNS-related barycentric field aligned with the free-jet shear layer as a whole (the IISRSM-related result at this location is color-coded light-magenta). The corresponding DNS/IISRSM trajectory data point lies exactly on the plane strain line characterized by $III_a = 0$. Finally, the trajectory bends back toward the $3C \rightarrow 1C$ boundary, approaching the red-colored segment at the $1C$ triangle vertex as the inflow pipe wall is reached at the exit plane. The pipe-jet release into the impingement channel is characterized by high turbulence-intensity components originating from the inner-wall region of the pipe (cf. Fig. 10), which contribute significantly to the pronounced enhancement of anisotropy as A approaches zero (cf. Fig. 11). Accordingly, the dark-blue region in Fig. 13-left corresponds to the red-colored region at the pipe-wall edge in the barycentric coordinate field at $r/D = 0.5$ in Fig. 13-right. The correspondingly stronger anisotropy is consistent with the increasing differences among the Reynolds stress components at $r/D = 0.5$ (cf. Fig. 10).

At the onset of the wall jet region ($r/D = 1.0$), the starting 'wall-bounded' data point remains at the same map boundary ($2C \rightarrow 1C$); however, the wall point shifts toward the $1C$ limit. The shift of the wall-related trajectory point from the immediate impingement location at $r/D = 0.5$, marked by a tiny green strip in Fig. 13-right, to the location $r/D \geq 1.0$, indicated by a yellow strip in the same figure (see also the corresponding colors in the barycentric triangle), is clearly correlated with the strong local flow acceleration observed in the near-wall region between $r/D = 0.5$ and 1.0 (see Fig. 5-right and Fig. 8), which marks the transition from the central impact zone to the wall-jet region. The initial trajectory trend at $r/D = 1.0$, composed of a set of sparsely distributed data points in the immediate vicinity of the impingement plate, gradually inclines and shortly crosses the $III_a = 0$-related turbulence state. It remains within the yellow-coded region of the barycentric triangle, corresponding to the inner boundary of the wall-jet shear layer at $z/D \approx 0.01$. This region is characterized by a near-wall maximum of the radial Reynolds stress component $\overline{u_r' u_r'}$ and comparatively low values of the remaining stress components (cf. Fig. 10), resulting in an enhanced level of turbulence anisotropy. This is evidenced by the onset of a narrow, blue-colored region that locally expands at the impingement wall up to $z/D \approx 0.05$, indicating correspondingly lower values of the parameter A ($A \leq 0.5$, cf. Fig. 11). Subsequently, the (x_B, y_B) trajectory within the barycentric triangle deviates from this path and progresses toward the interior of the map, which is characterized by positive III_a values (indicated consecutively by the magenta and blue regions in Fig. 13-right). After reaching the dark-blue region surrounding the $3C$ turbulence state — where the impinging jet still exhibits a noticeable streamline curvature effect upon impact at $z/D \approx 0.4$ (corresponding to the outer boundary of the wall-jet shear layer, where the Reynolds stress components are significantly suppressed; see Fig. 10) — the trajectory turns left and returns toward the $2C$–$3C$ boundary. The subsequent downward progression of the trajectory along the $3C \rightarrow 2C$ edge of the map indicates a low-momentum flow field outside the wall-jet region. This state corresponds to the light-blue region in Fig. 13-right and is characterized by negative III_a values and a high A parameter (cf. the light-to-dark red region in Fig. 13-left with $A \geq 0.8$; see also Fig. 11). Finally, the trajectory terminates at the upper wall, corresponding to the $2C$ turbulence state. This state reflects the kinematic blocking effect of the immediate wall vicinity on the Reynolds stress field, with the A parameter approaching zero. This behavior is consistent with the suppression of turbulence intensity toward zero as the upper plate is approached (see Fig. 10). The state is indicated in green in Fig. 13-right and corresponds to the consecutive green and light-to-dark blue regions in Fig. 13-left.

It is furthermore interesting to analyze the immediate near-wall region of the wall jet between the radial locations $r/D = 1$ and 2. As can be seen from the Reynolds stress component distribution in Fig. 10, there is a clear increase in the near-wall maximum of the wall-parallel stress component $\overline{u_r' u_r'}$ at $z/D \approx 0.02$ (see the associated discussion for the flow physics underlying this phenomenon), while the remaining components retain comparatively low values. This growing disparity between the individual stress components directly contributes to the strengthening of anisotropy. The yellow-coded region in the wall vicinity in the barycentric coordinate field in Fig. 13-right corresponds to the lower bound of the barycentric anisotropy triangle, connecting the $2C$ and $1C$ vertices and characterizing a two-component anisotropic turbulence state. The associated enhancement of the anisotropy level is

further reflected by the complementary blue region in the immediate vicinity of the wall in Fig. 13-left, which is characterized by lower A-parameter value of $A \leq 0.4$ (cf. Fig. 11).

Considering the next three cross-sections at radial locations $r/D \geq 2.0$, which intersect the developing wall jet, the Reynolds stress anisotropy trajectories exhibit a qualitatively similar progression to the previously analyzed variation in turbulence anisotropy, as observed in both the DNS- and IISRSM-based flow fields. However, the upward and downward trajectory branches, which cross the plane-strain turbulence state denoted by $III_a = 0$ multiple times while progressing centrally through the barycentric triangle, shift closer to each other. After originating at the bottom wall, which typically represents the two-component turbulence state (colored green–yellow), the trajectory crosses a region in the barycentric anisotropy triangle characterized by a progressively varying mixture of magenta, and light-blue. This region represents the vertical extent of the wall jet as projected onto the barycentric coordinate field in Fig. 13-right. It lies near the center of the barycentric map interior, with the A-parameter value progressively increasing to $\approx 0.75 - 0.8$, as shown in Fig. 13-left. Subsequently, the trajectory continues upward along the $III_a = 0$-related turbulence anisotropy state, ultimately entering the dark-blue-colored region of the barycentric triangle. This region corresponds to the low-momentum flow outside the wall jet in Fig. 13-right and indicates a turbulence anisotropy state approaching the three-component isotropic turbulence limit $\rightarrow 3C$. The anisotropy trajectory then turns downward in the barycentric triangle, exhibiting a similar trend parallel to, but at some distance from, the $3C - 2C$ map boundary, and moving across the light-blue regions toward the horizontal line corresponding to the $2C$ anisotropic turbulence state. This behavior coincides with the vicinity of the upper channel wall, as indicated by the green-coded barycentric representation of turbulence anisotropy (Fig. 13-right). This clearly indicates a turbulence state corresponding to an A-parameter value of approximately ≤ 0.6, as reflected by the narrow region coded consecutively by green and light-to-dark blue along the upper wall in Fig. 13-left. As noted above, the anisotropy representation at all three radial locations is qualitatively similar; the main differences lie in the fact that the specifically colored regions become wider with increasing radial distance from the impingement region toward the channel outlet. The dark-blue-colored, horizontally extending plume-like region gradually occupies a larger portion of the channel cross-sectional area in Fig. 13-right. The corresponding turbulence state in this region is consistent with the area near the upper apex of the barycentric triangle, indicating proximity to the $3C$ isotropic turbulence state. This region of the flow field exhibits a certain degree of relaxation, characterized by an increasing asymmetry of the velocity profile, a decreasing wall-related velocity gradient, and low-intensity flow reversal above the wall-jet region (cf. Fig. 8). A systematic reduction in turbulence intensity, following its maximum at $r/D = 2.0$, is also observed (cf. Fig. 5-left). The corresponding Reynolds stress component distributions shown in Fig. 10 follow this trend, with all components decreasing systematically at approximately the same rate. This behavior leads to the preservation of consistently high values of the two-component anisotropy factor A, as indicated by the progressively widening red-colored region in Fig. 13-left (see also the near-unity maxima in the A profiles in Fig. 11). An exception occurs in the immediate vicinity of both the bottom and upper walls — highlighted in blue — where anisotropy strengthening further occurs.

Despite some evident deviations, the agreement between the DNS and IISRSM results is satisfactory, considering the high sensitivity of interpreting the turbulence states through barycentric coloring and tracking of Reynolds stress anisotropy trajectories within the flow domain. Even small discrepancies in the Reynolds stress distribution (see Fig. 10) can lead to significant deviations in anisotropy-related parameters.

6. Conclusions

A complementary experimental and computational study of a round jet impinging perpendicularly onto a smooth wall is performed, involving PIV measurements, DNS, and RANS-based eddy-resolving turbulence modeling. The study examines the mean flow topology and the associated turbulence correlations in terms of the Reynolds stress components. The experimentally and computationally obtained results exhibit a high level of mutual agreement. The study captures a pronounced increase in turbulence level during the impingement process, driven by the destabilizing effect of local streamline curvature resulting from the 90-degree deflection of the downward free jet into the radially spreading wall jet. The directional change of the flow stream causes the streamwise turbulence intensity component of the free jet to transfer into the wall-normal component within the impingement zone, thereby redistributing the turbulent kinetic energy into the streamwise Reynolds stress component in the wall-jet formation region. In the early development of the wall jet, the flow acceleration at its onset leads to an enhanced velocity gradient in the shear layer zone, which further intensifies turbulence activity; subsequently, the turbulence levels associated with both the near-wall and shear-layer maxima exhibit a gradual decay. Although the results obtained at a Reynolds number of 10000 and a nozzle-to-wall distance of $z/D = 2$ may appear case-specific, the underlying flow physics and associated modeling challenges are representative of a broader range of Reynolds numbers and nozzle-to-plate distances. In particular, the global flow characteristics — especially the intensity of the acceleration and deceleration processes in the immediate impingement region — remain similar, as they are governed by the curvature of the streamlines induced by jet deflection. This observation is consistent with the findings of complementary experimental and numerical studies by Cooper et al. (1993) and Craft et al. (1993), which demonstrate a high degree of qualitative similarity in the profiles of normalized mean velocity and turbulent quantities for round jet impingement configurations operating at different Reynolds numbers and nozzle-to-wall distances.

A substantial part of the study is devoted to the representation of Reynolds stress anisotropy using both Lumley's anisotropy invariant theory and its barycentric mapping, thereby highlighting the characterization of turbulence states in terms of anisotropy parameterization. In addition to the spatial reproduction of the two-component parameter A across its full value range within the computational domain, characteristic anisotropy-dependent turbulence states are directly projected onto the physical flow field using the corresponding barycentric coloring. Accordingly, high close-to-unity values of the A parameter, indicating weak anisotropy, are characteristic of immediate impingement zone as well as the shear layer regions separating the free and wall jets from the low-momentum surrounding flow. In general, the turbulence structure remains narrowly bounded between the two-component isotropic limit $2C$ and the three-component, fully isotropic state $3C$, with most computational data points clustered along the left boundary of the Reynolds stress anisotropy invariant map. This behavior reflects the axisymmetric contraction state of turbulence and is consistent with the negative values of the third invariant of the Reynolds stress anisotropy tensor. The growing imbalance among the individual Reynolds stress components from the wall-jet onset location at $r/D = 1$ to the downstream position at $r/D = 2$, within the near field of wall-jet development, is accompanied by a pronounced increase in the near-wall peak of the wall-parallel stress component at a wall distance of $z/D \approx 0.01 - 0.02$, whereas the other components remain negligibly small. This evolution enhances the degree of anisotropy and reflects a turbulence state approaching the lower edge of the barycentric anisotropy triangle, which connects the $2C$ and $1C$ limiting states, thereby indicating a predominantly two-component anisotropic turbulence state in this region.

CRediT authorship contribution statement

M. Bopp: Writing – review & editing, Writing – original draft, Visualization, Validation, Software, Resources, Methodology, Investigation, Formal analysis, Data curation, Conceptualization. **T. Häber:** Writing – review & editing, Writing – original draft, Visualization, Validation, Supervision, Software, Resources, Methodology, Investigation, Formal analysis, Data curation, Conceptualization. **F. Secchi:** Writing – review & editing, Writing – original draft, Visualization, Validation, Software, Resources, Methodology, Investigation, Formal analysis, Data curation, Conceptualization. **S. Schulz:** Software, Methodology, Investigation, Formal analysis, Data curation, Conceptualization. **S. Wegt:** Software, Methodology. **L. Krüger:** Software, Methodology. **R. Suntz:** Writing – review & editing, Validation, Supervision, Resources, Project administration, Funding acquisition, Conceptualization. **D. Trimis:** Writing – review & editing, Supervision, Resources, Project administration, Funding acquisition, Conceptualization. **B. Frohnapfel:** Writing – review & editing, Writing – original draft, Visualization, Validation, Supervision, Resources, Project administration, Methodology, Funding acquisition, Formal analysis, Conceptualization. **S. Jakirlić:** Writing – review & editing, Writing – original draft, Visualization, Validation, Supervision, Resources, Project administration, Methodology, Funding acquisition, Formal analysis, Conceptualization.

Declaration of competing interest

The authors declare that they have no known competing financial interests or personal relationships that could have appeared to influence the work reported in this paper.

Acknowledgments

The financial support of the German Research Foundation (DFG) in the framework of the Collaborative Research Center/Transregio 150 (project number 237267381) is gratefully acknowledged. The authors furthermore would like to thank for the computing time granted on the Lichtenberg HPC at TU Darmstadt. The direct numerical simulations were performed on the HPE Apollo (Hawk) supercomputer at the High Performance Computing Center Stuttgart (HLRS) under the grant number 44198. T. Häber gratefully acknowledges the financial support by the Helmholtz Association of German Research Centers (HGF), Germany, within the research field MTET (Materials and Technologies for the Energy Transition), subtopic 'Technical Fuel Assessment' (38.03.04).

Appendix. 2D interpretation of turbulence anisotropy

With reference to the discussion about considering the experimentally determined flow fields in the turbulence anisotropy representation at the beginning of Section 5, this appendix presents a result related to the two-component anisotropy parameter A, which was obtained by taking into account the results of all three methods used. Accordingly, Fig. A.15 shows the field of the quantity $1 - \|a_{ij}\|_F$, where $\|a_{ij}\|_F$ denotes the Frobenius norm of the two-dimensional Reynolds stress anisotropy tensor field $(a_{ij})_{2D}$. The corresponding 2D matrix comprises only the components active in the central vertical plane $r - z$, namely a_{rr}, a_{zz}, and a_{rz} (with $a_{\theta\theta} = 0$ and $a_{rr} + a_{zz} = 0$, resulting from the zero trace of the corresponding 2D matrix). It is recalled that, in the PIV data, regions of the flow field where reliable measurements cannot be obtained are masked out. This is due to the fact that only the jet itself is seeded with particles, and the flow structure at the nozzle exit is not confined by a plate, unlike in the simulations. The fields obtained using the different methods show a high level of mutual agreement and are consistent with the two-dimensional interpretation of the two-component anisotropy parameter A_{2D}, which qualitatively closely follows the result obtained when accounting for the three-dimensional Reynolds stress anisotropy variation, as illustrated in Fig. 13-left.

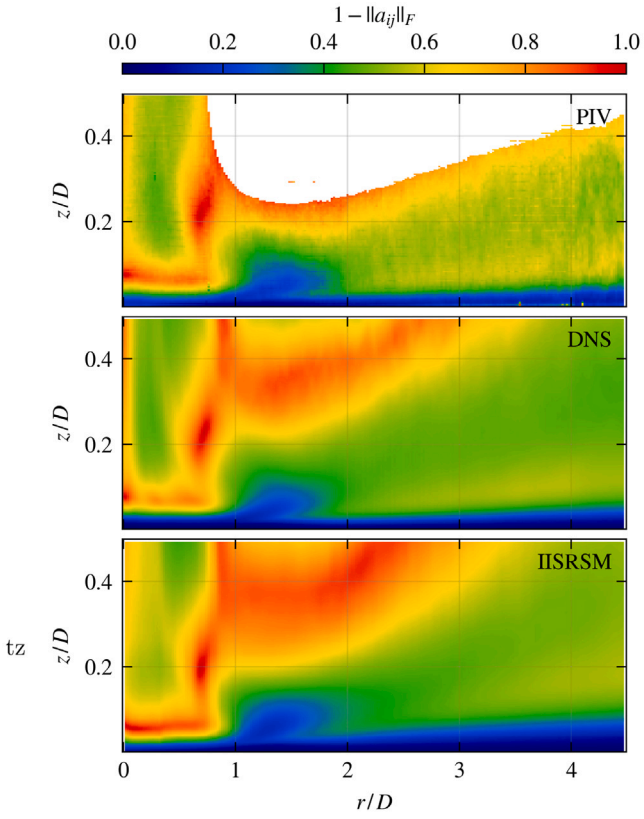

Fig. A.15. This figure relates to the A_{2D} two-component anisotropy parameter field, which is consistent with the corresponding variation of the Frobenius norm, $1 - \|a_{ij}\|_F$, of the two-dimensional Reynolds stress anisotropy tensor field $(a_{ij})_{2D}$.

Data availability

Data will be made available on request.

References

[1] D. Cooper, D. Jackson, B.E. Launder, G. Liao, Impinging jet studies for turbulence model assessment — I. Flow-field experiments, Int. J. Heat Mass Transf. 36 (10) (1993) 2675–2684, http://dx.doi.org/10.1016/S0017-9310(05)80204-2.

[2] T. Craft, L. Graham, B.E. Launder, Impinging jet studies for turbulence model assessment — II. An examination of the performance of four turbulence models, Int. J. Heat Mass Transf. 36 (10) (1993) 2685–2697, http://dx.doi.org/10.1016/S0017-9310(05)80205-4.

[3] M. Bopp, S. Wegt, L. Krüger, F. Secchi, B. Frohnapfel, S. Jakirlić, Flow and thermal fields modeling in jet impingement configurations using a Reynolds stress turbulence closure within the RANS and sensitized-RANS framework, Int. J. Heat Fluid Flow 105 (2024) 109264, http://dx.doi.org/10.1016/j.ijheatfluidflow.2023.109264.

[4] M. Hadžiabdić, K. Hanjalić, Vortical structures and heat transfer in a round impinging jet, J. Fluid Mech. 596 (2008) 221–260, http://dx.doi.org/10.1017/S002211200700955X.

[5] T. Dairay, V. V. Fortuné, E. Lamballais, L.E. Brizzi, LES of a turbulent jet impinging on a heated wall using high-order numerical schemes, Int. J. Heat Fluid Flow 50 (2014) 177–187, http://dx.doi.org/10.1016/j.ijheatfluidflow.2014.08.001.

[6] H. Hattori, Y. Nagano, Direct numerical simulation of turbulent heat transfer in plane impinging jet, Int. J. Heat Fluid Flow 25 (5) (2004) 749–758, http://dx.doi.org/10.1016/j.ijheatfluidflow.2004.05.004.

[7] T. Dairay, V. V. Fortuné, E. Lamballais, L.E. Brizzi, Direct numerical simulation of a turbulent jet impinging on a heated wall, J. Fluid Mech. 764 (2015) 362–394, http://dx.doi.org/10.1017/jfm.2014.715.

[8] J.L. Lumley, G.R. Newman, The return to isotropy of homogeneous turbulence, J. Fluid Mech. 82 (1) (1977) 161–178, http://dx.doi.org/10.1017/S0022112077000585.

[9] S. Banerjee, R. Krahl, F. Durst, C. Zenger, Presentation of anisotropy properties of turbulence, invariants versus eigenvalue approaches, J. Turbul. 8 (32) (2007) 1–29, http://dx.doi.org/10.1080/14685240701506896.
[10] M. Emory, G. Iaccarino, Visualizing turbulence anisotropy in the spatial domain with componentality contours, in: Annual Research Brief, Center for Turbulence Research, Stanford University, 2014, pp. 123–138, URL: https://web.stanford.edu/group/ctr/ResBriefs/2014/14_emory.pdf.
[11] M. Hasenzahl, S. Jakirlic, C. Hasse, Mean velocity scaling in the turbulent piston boundary layer of a motored IC engine, Theor. Appl. Mech. Lett. 16 (2026) 100667, http://dx.doi.org/10.1016/j.taml.2026.100667.
[12] P.C. Ma, T. Ewan, C. Jainski, L. Lu, A. Dreizler, V. Sick, M. Ihme, Development and analysis of wall models for internal combustion engine simulations using high-speed micro-PIV measurements, Flow, Turbul. Combust. 98 (2017) 283–309, http://dx.doi.org/10.1007/s10494-016-9734-5.
[13] M. Raffel, C.E. Willert, S.T. Wereley, J. Kompenhans, Particle Image Velocimetry: A Practical Guide, second ed., Springer Berlin Heidelberg, Berlin, Heidelberg, 2007, http://dx.doi.org/10.1007/978-3-540-72308-0, URL: http://swbplus.bsz-bw.de/bsz272959790cov.htm.
[14] S. Scharnowski, C.J. Kähler, Particle image velocimetry - classical operating rules from today's perspective, Opt. Lasers Eng. 135 (2020) 106185, http://dx.doi.org/10.1016/j.optlaseng.2020.106185.
[15] P.J. Rousseeuw, A.M. Leroy, Robust Regression and Outlier Detection, John Wiley & Sons, Inc, Hoboken, NJ, USA, 1987, http://dx.doi.org/10.1002/0471725382.
[16] J. Westerweel, Efficient detection of spurious vectors in particle image velocimetry data, Exp. Fluids 16–16 (3–4) (1994) 236–247, http://dx.doi.org/10.1007/BF00206543.
[17] M. Templ, J. Gussenbauer, P. Filzmoser, Evaluation of robust outlier detection methods for zero-inflated complex data, J. Appl. Stat. 47 (7) (2020) 1144–1167, http://dx.doi.org/10.1080/02664763.2019.1671961.
[18] S. Jakirlić, K. Hanjalić, A new approach to modelling near-wall turbulence energy and stress dissipation, J. Fluid Mech. 459 (2002) 139–166, http://dx.doi.org/10.1017/S0022112002007905.
[19] F. Menter, Y. Egorov, The scale-adaptive simulation method for unsteady turbulent flow predictions. Part 1: theory and model description, Flow Turbul. Combust. 85 (1) (2010) 113–138, http://dx.doi.org/10.1007/s10494-010-9264-5.
[20] J.C. Rotta, Turbulente Strömungen. Eine Einführung in die Theorie und ihre Anwendung, Verlag B.G. Teubner Stuttgart, 1972, p. 266, http://dx.doi.org/10.1007/978-3-322-91206-0.
[21] X. Wang, J. Hussong, S. Jakirlić, Curvature influence on flow and heat transfer in a concentric annulus: Conventional and sensitized Reynolds stress modeling study, Int. J. Heat Mass Transfer 249 (2025) 127192, http://dx.doi.org/10.1016/j.ijheatmasstransfer.2025.127192.
[22] X. Wang, J. Hussong, S. Jakirlić, Combined effects of Reynolds number and particle mass loading on secondary flow patterning in a horizontal pipe: a sensitized RANS-RSM study, 2026, http://dx.doi.org/10.2139/ssrn.6657818, SSRN. URL: https://ssrn.com/abstract=6657818.
[23] S. Jakirlić, R. Maduta, Extending the bounds of 'steady' RANS closures: Toward an instability-sensitive Reynolds stress model, Int. J. Heat Fluid Flow 51 (2015) 175–194, http://dx.doi.org/10.1016/j.ijheatfluidflow.2014.09.003.
[24] X. Wang, J. Hussong, S. Jakirlić, Eddy-resolving Reynolds stress modeling of particle-laden flows using a multiphase Euler-Lagrange approach, Int. J. Heat Fluid Flow 115 (2025) 109853, http://dx.doi.org/10.1016/j.ijheatfluidflow.2025.109853.
[25] I. Maden, R. Maduta, J. Kriegseis, S. Jakirlić, C. Tropea, Plasma-actuated manipulation of secondary flow towards pressure recovery enhancement in a 3D diffuser modelled by an eddy-resolving second-moment closure, Flow Turbul. Combust. 95 (2015) http://dx.doi.org/10.1007/s10494-015-9641-1.
[26] R. Maduta, M. Ullrich, S. Jakirlić, Reynolds stress modelling of wake interference of two cylinders in tandem: Conventional vs. eddy-resolving closure, Int. J. Heat Fluid Flow 67 (2017) 139–148, http://dx.doi.org/10.1016/j.ijheatfluidflow.2017.07.012.
[27] A. Bauer, M. Bopp, S. Jakirlić, C. Tropea, A.J. Krafft, N. Shokina, J. Hennig, Analysis of the wall shear stress in a generic aneurysm under pulsating and transitional flow conditions, Exp. Fluids 61 (2020) http://dx.doi.org/10.1007/s00348-020-2901-4.
[28] M. Ullrich, B. Krumbein, R. Maduta, S. Jakirlić, Turbulent flow in a square cross-sectioned bubble column computed by a scale-resolving Reynolds-stress model, Chem. Eng. Sci. 230 (2021) 116201, http://dx.doi.org/10.1016/j.ces.2020.116201.
[29] I. Joksimović, T. Čorbo, J. Hussong, S. Jakirlić, Secondary flow and thermal field dynamics in a T-junction with an upstream elbow: A POD-aided, eddy-sensitized Reynolds-stress modeling study, Int. J. Heat Fluid Flow 104 (2023) 109226, http://dx.doi.org/10.1016/j.ijheatfluidflow.2023.109226.
[30] I. Joksimović, S. Jakirlić, Eddy-resolving Reynolds-stress modeling of thermal mixing in cross-stream type T-junction configurations, Appl. Therm. Eng. 235 (2023) 121390, http://dx.doi.org/10.1016/j.applthermaleng.2023.121390.
[31] M.M. Gibson, B.E. Launder, Ground effects on pressure fluctuations in the atmospheric boundary layer, J. Fluid Mech. 86 (3) (1978) 491–511, http://dx.doi.org/10.1017/S0022112078001251.
[32] S. Jakirlic, K. Hanjalic, A DNS-based re-examination of coefficients in the pressure-strain models in second-moment closures, Fluid Dyn. Res. 45 (5) (2013) 055509, http://dx.doi.org/10.1088/0169-5983/45/5/055509.
[33] S. Dong, A convective-like energy-stable open boundary condition for simulations of incompressible flows, J. Comput. Phys. 302 (2015) 300–328, http://dx.doi.org/10.1016/j.jcp.2015.09.017.
[34] P. Fisher, J. Lottes, S. Kerkemeier, NEK5000 Version 19.0, Argonne National Laboratory, Illinois, 2008-2020, https://nek5000.mcs.anl.gov/.
[35] Y. Maday, A. Patera, Spectral element methods for the incompressible Navier-Stokes equations, in: A. Noor (Ed.), State of the Art Surveys on Computational Mechanics. ASME, New York, 1989, pp. 71–143.
[36] Y. Maday, A. Patera, E. Rønquist, An operator-integration-factor splitting method for time-dependent problems: Application to incompressible fluid flow, J. Sci. Comput. 5 (1990) 263—-292, http://dx.doi.org/10.1007/BF01063118.
[37] P. Hoffmann, K. Muck, P. Bradshaw, The effect of concave surface curvature on turbulent boundary layers, J. Fluid Mech. 161 (1985) 371–403, http://dx.doi.org/10.1017/S0022112085002981.
[38] R.D. Moser, P. Moin, The effects of curvature in wall-bounded turbulent flows, J. Fluid Mech. 175 (1987) 479–510, http://dx.doi.org/10.1017/S0022112087000491.
[39] M. Schmidt, C.-P. Ding, B. Peterson, A. Dreizler, B. Böhm, Near-wall flame and flow measurements in an optically accessible SI engine, Flow Turbul. Combust. 106 (2) (2021) 597–611, http://dx.doi.org/10.1007/s10494-020-00147-9.
[40] A. Nicolas, F. Zentgraf, M. Linne, A. Dreizler, B. Peterson, Assessment and application of wavelet-based optical flow velocimetry (wOFV) to wall-bounded turbulent flows, Exp. Fluids 64 (3) (2023) 51–73, http://dx.doi.org/10.1007/s00348-023-03594-y.
[41] K.S. Choi, J.L. Lumley, The return to isotropy of homogeneous turbulence, J. Fluid Mech. 436 (2001) 59–84, http://dx.doi.org/10.1017/S002211200100386X.